Acta Astronautica 155 (2019) 426–447

Contents lists available at ScienceDirect

Acta Astronautica

journal homepage: www.elsevier.com/locate/actaastro

Safety analysis for shallow controlled re-entries through reduced order modeling and inputs' statistics method

S.F. Rafano Carná, S. Omar, D. Guglielmo, R. Bevilacqua*

University of Florida, MAE-A 211, 939 Sweet Water Drive, Gainesville, FL, 32611, USA

ARTICLE INFO

Keywords:
Ground population risk assessment
Re-entry safety analysis
Safety boxes
Inputs' statistics
Reduced order model
Drag de-orbit device

ABSTRACT

In recent years, the interest and demand for small satellites have grown exponentially. While in the past the end-of-life design for this type of spacecraft was often approximated or totally neglected, it has recently become increasingly important. Indeed, small spacecraft able to achieve advanced mission objectives are more frequently on the worldwide space agenda. They may contain components which might withstand the re-entry conditions and reach the ground. In addition, these spacecraft are usually limited to shallow re-entries which are more sensitive to atmospheric model uncertainties and thus have larger debris fields. The objective of this work is to provide a reliable and efficient statistical analysis to estimate the risk to aeronautic and maritime traffic as well as to ground based populations. A simple geometric safety assessment is proposed, based on the safety boxes concept introduced in the ESA Space Debris Mitigation Compliance Verification Guidelines. Correctly estimating the dimensions of a safety box and locating it over uninhabited regions, such as the oceans, guarantees a casualty risk below a prescribed value. Furthermore, by estimating the probability of debris landing outside the largest possible safety box within which there is a zero casualty risk, the maximum probability of control failure admissible for the mission can be estimated. This proposed safety analysis is achieved using two re-entry models of differing complexity. The high fidelity model includes both the aerodynamic and aerothermodynamic effects that occur during re-entry and is used to statistically characterize "high level" uncertain variables such as the ballistic coefficient and the demise altitude. The reduced order model is based on these high level variables and captures the spacecraft fragmentation behavior and its re-entry dynamics with significantly less computation time than the high fidelity model. Coupled with advanced statistical techniques designed to estimate very low probabilities such as the Inputs' Statistics Method, a reliable safety analysis can be conducted with a limited overall computational burden. The proposed safety analysis is applied to a fictitious 2U CubeSat mission that performs a controlled re-entry using the Drag De-orbit Device developed by the ADAMUS laboratory at the University of Florida.

1. Introduction

Whenever a spacecraft mission is launched where the satellite will re-enter the atmosphere at the end of the mission, it is necessary to asses the risk that re-entering debris will pose to persons or property on the ground [1]. For satellites launched in the United States, NASA's Debris Assessment Software (DAS) [2] is frequently utilized to estimate an upper bound on the probability of human casualty associated with an uncontrolled satellite re-entry. Other countries have different software packages and regulations [3], but in any case, the casualty risk associated with the re-entering debris of a given mission must not exceed a specified value.

While most small satellites such as CubeSats [4] do not exceed the maximum casualty risk when re-entering without control, the advancement and miniaturization of technology has resulted in satellites too small to contain thrusters but containing instruments made of materials such as tungsten or titanium that will survive re-entry. In addition, the increasing number of satellites being launched will likely lead to a decrease in the acceptable casualty probability per satellite. For satellite missions that exceed the acceptable casualty risk associated with an un-controlled re-entry, it is necessary to control the de-orbit point of the satellite to ensure that the debris land in an unpopulated are such as the South Pacific Ocean Uninhabited Area (SPOUA) [5].

When a controlled re-entry is required, a detailed analysis of the spacecraft re-entry profile is necessary to assess compliance with the debris mitigation guidelines. To do this, object oriented analysis

* Corresponding author.
E-mail addresses: s.rafanocarna@ufl.edu (S.F.R. Carná), sanny.omar@ufl.edu (S. Omar), dguglielmo@ufl.edu (D. Guglielmo), bevilr@ufl.edu (R. Bevilacqua).

https://doi.org/10.1016/j.actaastro.2018.10.015
Received 28 December 2017; Received in revised form 17 September 2018; Accepted 8 October 2018
Available online 12 October 2018

software such as NASA's ORSAT [6,7] and spacecraft oriented analysis software such as ESA's SCARAB [8] have traditionally been used. Spacecraft oriented approaches require a detailed computer model of the satellite where the behavior of each specific spacecraft component during the re-entry is considered. Object oriented approaches model the satellite as a combination of simple objects (cubes, spheres, etc.) that when simulated along a re-entry trajectory, yield a debris profile similar to that of the real satellite. Often, the spacecraft behavior simulated using the spacecraft oriented approach is utilized to determine the set of parameters (e.g. demise altitude) and their statistical characterizations that should be utilized in the more computationally efficient object oriented simulation [9]. By conducting Monte Carlo simulations with the object oriented tool, a statistical characterization of the debris field generated by the satellite can be determined. This debris field will be dependent on the physical properties of the satellite, the expected initial conditions of the re-entry trajectory, and the uncertainties of the environmental conditions.

Unfortunately, software packages such as ORSAT and SCARAB are tightly controlled by NASA and ESA and can generally be used by spacecraft builders only as analysis tools rather than design tools. That is, the mission designer would specify to NASA or ESA the characteristics of their spacecraft and the expected re-entry initial conditions, and they would be told whether the spacecraft is compliant with the debris guidelines or not without receiving detailed information about the inner workings or numerical results of SCARAB or ORSAT. For large satellite missions, a propulsive de-orbit burn is generally conducted, so the re-entry trajectory will be steep, the debris footprint will be much smaller than for a shallow re-entry [10], and the satellite operator will be confident that the satellite is compliant with debris guidelines prior to running any analysis. SCARAB or ORSAT can then be used to verify that the spacecraft is indeed compliant. However, for some missions, an iterative analysis of the re-entry profile may be an important part of the design process.

Recent studies have shown that controlling the de-orbit location of a spacecraft using solely aerodynamic drag is feasible [11–14] and several retractable drag devices are in development to enable a spacecraft to perform this controlled re-entry [15,16]. This paper specifically investigates the case of a 2U CubeSat attached to the Drag De-orbit Device (D3) being developed by the University of Florida Adavanced Autonomous Multiple Spacecraft Lab [15], but the approaches discussed can be generalized to any satellite. Drag-controlled re-entries, in general, will be much shallower than propulsive re-entries, so the debris footprints will be much larger. For this reason, the debris profile must be carefully analyzed, and the targeted de-orbit point must be optimized to minimize the casualty risk associated with the debris profile. While there is published information on modeling the aerothermodynamic properties of re-entering spacecraft [17,18], the existing literature, aside from Ref. [19], does not contain a comprehensive study of the relations required to implement a high fidelity spacecraft re-entry model. In addition, there is no existing publicly available analysis of the debris profile of a satellite that is based on both the re-entry aerothermodynamics and the expected initial condition errors resulting from de-orbit point targeting using aerodynamic drag. There is also not a well defined methodology of selecting the optimal de-orbit point and determining the performance of a drag controlled satellite required to meet the debris mitigation guidelines.

Section 2 of this paper begins by briefly describing the high fidelity re-entry model that is detailed in Ref. [19]. This model accurately computes the behavior and thermal profile during the re-entry of a rectangular-shaped satellite possibly equipped with the D3 device. In sec. 3, the statistical distributions of the variables used in the high fidelity model are discussed. This includes the aerodynamic and aerothermodynamic variables (sec. 3.2) as well as the expected distributions on the orbital conditions at de-orbit point achieved through the targeting algorithm in Ref. [11] (sec. 3.1). A reduced order model discussed in sec. 4 is derived which contains far fewer input variables than the high fidelity model. This model can be utilized to rapidly run many simulations that capture the spacecraft re-entry profile specified by the high fidelity model with a significantly lower computational burden. Once the reduced order model is developed, the detailed debris mitigation requirements are discussed in sec. 5 along with a method of ensuring compliance with the requirements. The compliance method involves the calculation of safety boxes (sec. 6) using the novel and computationally efficient Inputs' Statistics Method such that the probability that a spacecraft fragment lands outside the safety box is below a prescribed value. Next, sec. 7 provides a method of selecting the optimal de-orbit point such that the safety box lies in the middle of the SPOUA and is as far away as possible from land, minimizing the risk from falling debris. Finally, given the nominal casualty risk from uncontrolled re-entry and a desired altitude below which the spacecraft decay trajectory will be uncontrolled, sec. 8 provides a method of calculating the maximum allowable probability of failure of the controlled re-entry process such that the spacecraft remains compliant with a given debris mitigation requirement. Overall, this paper provides a comprehensive method for analyzing the expected debris profile from a drag-controlled satellite mission and provides tools that allow satellite builders to design the end-of-life mission plan such that the risk from re-entering debris is minimized.

2. High fidelity model of the re-entry

Three necessary building blocks have to be implemented to characterize the evolution of the spacecraft dynamics to a potential ground impact: the aerodynamic model, the aerothermodynamic model, and the dynamic model of the spacecraft [20]. The aerodynamic model gives an estimation of the drag force acting on the vehicle, characterized as the exchange of momentum between it and the surrounding flow [17]. The aerothermodynamic model calculates the heat power that enters into the structure due to the fact that air flows at high speed around the spacecraft [21]. The aerodynamic model and the aerothermodynamic model are nested inside the dynamic model and ultimately provide it with the estimation of two key parameters: the drag coefficient and the heat power at the outside of the spacecraft, respectively. Finally, the dynamic model provides the trajectory followed by the spacecraft as position and velocity values over time through the integration of the equations of motion [22].

The choice of the specific mathematical law to characterize the key parameters depends on 1) the flowfield regime, determined through the Knudsen number and the Mach number, 2) the assumption and underlying hypothesis selected for the specific problem, and 3) by the spacecraft nose geometry. Semi-analytical laws and correlations, developed in the literature [18,21,23–29], can be used in order to avoid time-consuming CFD-based calculations. Unfortunately, most of these models are derived in dated and difficult-to-access papers and technical reports, each using a completely different nomenclature and notation. They are based on specific assumptions, which are often not mutually compatible. Therefore, we decided to develop a comprehensive work [19], recently accepted for publication, that includes all the necessary and sufficient laws, data, and correlations to describe the re-entry of small satellites. The selected laws are consistent in their assumptions and approximations. They are presented in an organized fashion and with a uniform nomenclature in order to provide the reader with a tool that is easy to understand and implement. We encourage the reader to refer to ref. [19] for all the details. Here, we include only the tables that specify the correlations for the modeled 2U CubeSat (Table 1) and the attached drag device (Table 2). This Drag De-Orbit Device (D3) consists of four repeatedly retractable tape-spring booms that deploy to a length of 3.7 m to expedite orbital decay and facilitate orbital maneuvering and controlled re-entry using the algorithms in ref.[12, 11]. The details of the D3 are discussed in Ref. [30]. The CubeSat is assumed to re-enter the atmosphere with the D3 booms deployed to a specified level (0.5 m^2 in this paper), and at some point during the re-entry, the D3 booms will

Table 1
Summary of all the correlations used in the aerodynamic and aerothermodynamic models.

			Aero-dynamic model	Aerothermo-dynamicmodel
Free molecular regime $Kn > 10$			Schaaf and Chambre's analytic model [26]	
Transition regime $0.01 < Kn < 10$			Wilmoth's bridging law [37]	Legge's bridging law [24]
Continuum regime $Kn < 0.01$	Hypersonic regime $Ma > 10$	Blunt nose	Modified Newton Law [27]	Fay and Riddel's correl [28].
		Sharp nose	Newton Law [17,57]	Eckert's model [29]
	Hypersonic-supersonic transition $2 < Ma < 10$	Blunt nose	Sigmoid bridging formula	Fay and Riddel's correl [28]. if $Ma > 6$ or else no heat [8]
		Sharp nose	Sigmoid bridging formula	Eckert's model [29] if $Ma > 6$ or else no heat [8]
	Low Mach number $Ma < 2$		Hulburt's data [58]	No heat [8]

melt, bend due to the aerodynamic force, or both.

The simulation of the re-entry of the CubeSat equipped with the D3 device is set up as illustrated in Fig. 1. The numerical propagation starts from a prescribed de-orbit point (DEO point) at the geodetic altitude h_{DEO}. Since the D3 provides 3-axis stabilization with the 1U face of the CubeSat pointing in the velocity direction (named HW face pointing mode in Ref. [19]), the spacecraft is assumed to maintain this attitude during the initial part of the re-entry. The D3 booms are deployed with a predetermined length of 0.5 m. Their bending stiffness has been designed in order to withstand a maximum torque C^{Max} of about $0.35Nm$. Therefore, the booms are expected to bend at an altitude of about 95 km, as estimated in Ref. [19]. When the aerodynamic force is large enough that the boom bending torque is exceeded, the D3 booms are considered fully bent and parallel to the flow, contributing to the drag force only through shear stress with the surrounding flow. When the D3 booms melt, the trajectory of the sole CubeSat is propagated in a tumbling mode. The numerical simulation proceeds until the spacecraft melting condition is reached.

In the re-entry scenario, two possible situations may occur:

- if the D3 booms bend before melting (Fig. 1a), the geodetic altitude at which this event occurs is recorded as bending altitude h_{Bend}. Then, the D3 booms are considered aligned with the flow. Since the center of pressure is still behind the center of mass, they continue to provide stabilization in the HW face pointing mode. The integration proceeds up to the CubeSat structure demise altitude h_{Dem}.
- If the D3 booms melt before bending (Fig. 1b), the geodetic altitude at which this event occurs is recorded as the D3 demise altitude h_{D3Dem}. Then, the integration proceeds considering the CubeSat only, in tumbling mode, up to its demise at h_{Dem}.

From the spacecraft demise altitude to the ground impact point, the trajectory of a single debris fragment is propagated with a specified

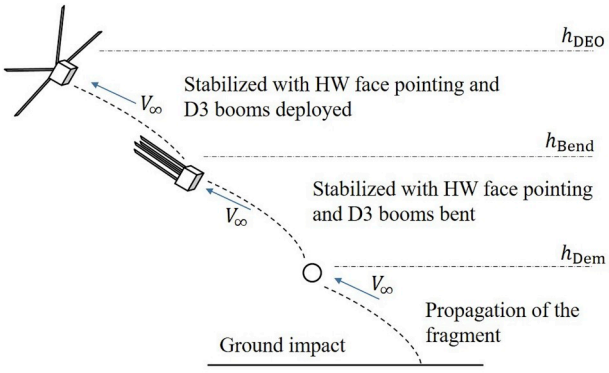

(a) Phases if the D3 booms bend before melting.

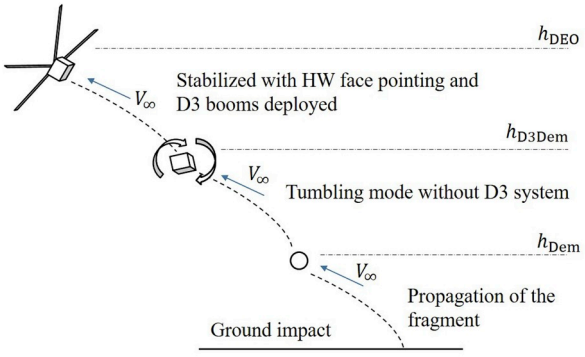

(b) Phases if the D3 booms melt before bending.

Fig. 1. Different phases of the simulation.

Table 2
Summary of all the correlations used in the aerodynamic and aerothermodynamic models of the D3 system.

			Aero-dynamic model	Aerothermo-dynamicmodel
Free molecular regime $Kn > 10$			Schaaf and Chambre's analytic model [26]	
Transition regime $0.01 < Kn < 10$			Wilmoth's bridging law [37]	
Continuum regime $Kn < 0.01$	Hypersonic and supersonic regime $Ma > 2$	Deployed	Modified Newton Law [27]	Fay and Riddel's correl [28]. if $Ma > 6$ or else no heat [8]
		Bent	Li and Nagamatsu theory [38]	Fay and Riddel's correl [28]. if $Ma > 6$ or else no heat [8]
	Low Mach number $Ma < 2$		Not of interest	No heat [8]

ballistic coefficient. This represents the re-entry of a CubeSat containing an instrument made of a material such as tungsten or titanium that does not melt on re-entry.

3. Statistical characterization of the high fidelity model

As suggested by Renaud and Martin in Ref. [5], the uncertain variables for atmospheric re-entry may be grouped into three categories:

- spacecraft re-entry performances and initial conditions;
- environmental factors;
- break-up/explosion model.

In the first category, we include the guidance navigation and control (GNC) errors that inevitably result during the drag-controlled orbital decay of the spacecraft. Environmental uncertainties result from the imperfect nature of the selected atmospheric model and the inability to precisely predict future solar activity which influences the atmospheric density. Finally, in the case of a CubeSat re-entry, we do not expect a catastrophic explosion of the spacecraft due to the small amount of fuel on board. Rather, a slow and progressive fragmentation process is more likely to occur. This process is approximately captured by the aerothemodynamic model and thermal model of the spacecraft, as described in Ref. [19]. Nevertheless, there is always significant uncertainty in any model or correlation used. In the rest of this section, the choices of the statistical distributions for each uncertain variable are discussed.

3.1. GNC dispersions

The D3 system allows a host spacecraft to control its orbital decay and can be utilized with the algorithm in ref.[12, 11], hereafter called targeting algorithm, to reach a specific DEO point. In the targeting algorithm, the DEO point is defined as a longitude and geocentric latitude when the spacecraft crosses a specific geocentric altitude. Two sources of error result from the targeting algorithm: a tracking error and a guidance error. The guidance specifies a nominal trajectory that the spacecraft must follow to de-orbit in a desired location. Often, however, the algorithm is unable to calculate a guidance that brings the satellite precisely to the desired DEO point (guidance error). The tracking algorithm continuously modulates the spacecraft ballistic coefficient to ensure that the satellite remains on the guidance despite uncertainties in the estimated drag force. This tracker is not perfect however, and there will always be some discrepancy (tracking error) between the actual and desired satellite positions at a given point in time. The error between the desired DEO point and the actual DEO point obtained at the final point of the tracking trajectory is the overall (combined guidance and tracking) GNC error.

The DEO point becomes the initial condition for the propagation of the re-entry dynamics with the high fidelity model introduced in Section 2. Because of the GNC errors described above, the DEO point is not perfectly known, but it can be statistically characterized through a MC analysis. This analysis consists of a significant number of simulations of the guidance and the tracking of the targeting algorithm. The number of runs must be high enough to guarantee a specified confidence level and relative error [31]. To compute it, based on our experience with the targeting algorithm, the a priori assumption of having normally distributed errors is introduced. The Kolmogrov-Smirnov test [32] is used to justify a posteriori this choice and fails to reject to null hypothesis of normality with a confidence of $\alpha = .05$. Thus, with this assumption, we can estimate the confidence levels for the standard deviations σ of various uncertain variables as ([33]):

$$\frac{(N-1)\hat{\sigma}^2}{\chi^2_{(\alpha/2,N-1)}} \leq \sigma^2 \leq \frac{(N-1)\hat{\sigma}^2}{\chi^2_{(1-\alpha/2,N-1)}} \tag{1}$$

where N is the number of samples, $1-\alpha$ is the confidence level we want to achieve, $\hat{\sigma}$ is the sample standard deviation and $\chi^2_{(1-\alpha/2,N-1)}$ is the $(1-\alpha/2)$-quantile of the chi square distribution with $N-1$ degrees of freedom. Therefore, setting the half-width of the confidence level equal to the desired relative error RE and solving eq. (1) for N, we get the minimum required number of runs as:

$$N = 1 + \left(\frac{2\,RE}{\frac{1}{\sqrt{\chi^2_{(1-\alpha/2,N-1)}}} - \frac{1}{\sqrt{\chi^2_{(\alpha/2,N-1)}}}} \right)^2 \tag{2}$$

Eq. (2) is a non linear equation that can be solved with a classical root solver. In this case, relative error is defined as a percentage of the standard deviation. For consistency throughout the paper, we require a confidence level of 95% and a relative error of 10% and consequently we need to run at least 200 simulations. This confidence level means that if the 200-run MC campaign were repeated, there would be a 95% probability that the true standard deviation is within 10% of the standard deviation associated with the new MC runs.

Each simulation begins from the same typical ISS orbit (400 km altitude circular orbit inclined at 51.9°), but with a different initial epoch (and hence different density profile). The epoch is randomly varied between November 2003 and November 2014 to capture the density variations throughout the 11-year solar cycle. The same DEO point ($\lambda_{\mathrm{DEO}} = 99^{\circ}$ longitude, $\zeta_{\mathrm{DEO}} = 0^{\circ}$ geodetic latitude) is targeted in order to characterize the errors for a specific de-orbit scenario. Since the estimation of the on-ground dispersion of the fragments surviving the re-entry is driven by the number of uncertainties on the problem, these uncertainties must be reduced as much as possible. A large source of uncertainty exists on the altitude at which the D3 will be unable to modulate the booms due to heat-induced failures of the internal mechanisms. If the D3 booms fail in an unknown configuration, there will be significant uncertainty on the ballistic coefficient during re-entry resulting in large ground dispersions. Furthermore, a potential asymmetric failure condition may occur, giving rise to unforeseen aerodynamic stabilization conditions which cause the fragments to fall very far from expected. To eliminate this issue, the D3 device operations are shut down at a predetermined altitude high enough that heat-induced failure of the D3 is not a concern. The selected DEO altitude is $120km$ (geodetic) and the D3 booms are set to deploy with length of $0.5m$ at this altitude.

Using the final inertial state vector $\{\mathbf{R}, \mathbf{V}\}$ of the tracking trajectory, the GNC error at the DEO point can be expressed in terms of four key parameters which strongly affect the subsequent propagation of the re-entry dynamics: the along-track error $\upsilon_{//}$, the cross-track error $\upsilon_{\perp}$, the relative flight path angle γ, and the error on the magnitude of the relative velocity vector $\mathbf{v}$. More specifically, the relative velocity vector $\mathbf{v}$ is the velocity relative to the rotating atmosphere as defined in Vinh et al. [22] and computed as:

$$\mathbf{v} = \mathbf{V} - \boldsymbol{\omega}_{\oplus} \times \mathbf{R} \tag{3}$$

where $\boldsymbol{\omega}_{\oplus}$ is the rotational angular velocity vector of Earth. The relative flight path angle γ is the angle within the local vertical plane between $\mathbf{v}$ and the horizontal plane. It can be computed introducing two common reference frames (Fig. 2):

The *Earth-centred local* (ECL) reference frame, indicated by the three unit vectors $\{\mathbf{i}', \mathbf{j}', \mathbf{k}'\}$, and the *Vehicle-centred intrinsic* (VCI) reference frame, indicated by the three unit vectors $\{\mathbf{i}'', \mathbf{j}'', \mathbf{k}''\}$ [19,22]. They are defined as:

$$\mathbf{i}' = \frac{\mathbf{r}}{\|\mathbf{r}\|}; \quad \mathbf{j}' = \frac{\mathbf{k} \times \mathbf{i}'}{\|\mathbf{k} \times \mathbf{i}'\|}; \mathbf{k}' = \mathbf{i}' \times \mathbf{j}' \tag{4}$$

for the ECL frame and:

$$\mathbf{j}'' = \frac{\mathbf{v}}{\|\mathbf{v}\|}; \quad \mathbf{k}'' = \frac{\mathbf{i}' \times \mathbf{j}''}{\|\mathbf{i}' \times \mathbf{j}''\|}; \quad \mathbf{i}'' = \mathbf{j}'' \times \mathbf{k}'' \tag{5}$$

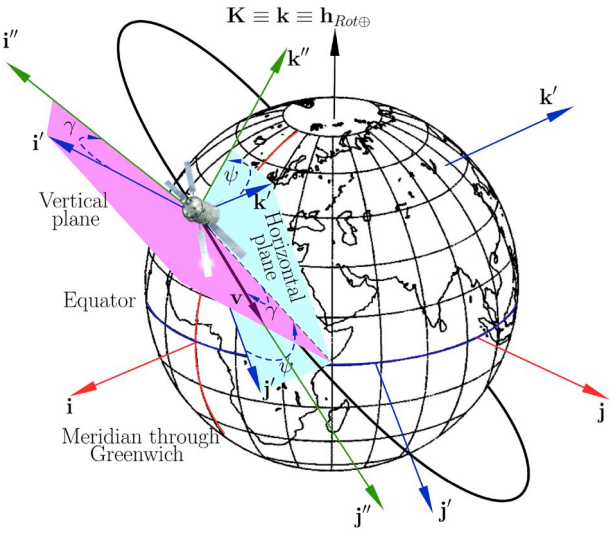

Fig. 2. Reference frames illustrations: Earth Centred Earth Fixed (ECEF) frame in red, Earth Centred Local (ECL) frame in blue and Vehicle centred Intrinsic (VCI) frame in green. (For interpretation of the references to colour in this figure legend, the reader is referred to the Web version of this article.)

for the VCI frame. The vector **k** is the north pole direction and **r** is the position vector direction, all expressed in the same reference frame as the relative velocity vector **v**. Thus, the flight path angle is computed as:

$$\gamma = \frac{\mathbf{v}\cdot\mathbf{i}'}{|\mathbf{v}\cdot\mathbf{i}'|}\cos^{-1}(\mathbf{i}'\cdot\mathbf{i}'') \tag{6}$$

The along track and cross track angle are introduced in order to reduce the correlation that actually exists in the data if they are directly dealt with in terms of latitude and longitude. They are computed projecting the position on a reference frame tangent to the ground track. The rotation angle θ between the tangent to the ground track at the DEO point and West-East direction of the normal Mercator projection is computed as:

$$\theta = \tan^{-1}(\tan\psi\cos\varphi) \tag{7}$$

where φ is the geocentric latitude and ψ is the relative heading angle. The heading angle is the angle in the local horizontal plane between the local parallel and the projection of the relative velocity vector **v** in the local horizontal plane, positively in the direction of motion (see Fig. 2). It can be computed as:

$$\psi = \frac{\mathbf{v}\cdot\mathbf{k}'}{|\mathbf{v}\cdot\mathbf{k}'|}\cos^{-1}(\mathbf{k}'\cdot\mathbf{k}'') \tag{8}$$

So, the along track $\upsilon_{//}$ and cross track $\upsilon_{\perp}$ errors are computed as:

$$\upsilon_{//} = \cos\theta\,(\lambda - \lambda_{\mathrm{DEO}}) + \sin\theta\,(\varphi - \varphi_{\mathrm{DEO}}) \tag{9}$$

$$\upsilon_{\perp} = -\sin\theta\,(\lambda - \lambda_{\mathrm{DEO}}) + \cos\theta\,(\varphi - \varphi_{\mathrm{DEO}}) \tag{10}$$

The numerical distributions of these four selected variables for the 200-run MC simulation are shown in Fig. 3. They are all approximated as normally distributed, with the exception of the cross track angular error. We find that a truncated Student's-*t* location scale distribution [33,34] is a better fit for cross-track error, as is also verified by the Kolmogrov-Smirnov test (Fig. 4). This is due to the outliers points that come from the more limited longitude controllability of the targeting algorithm [11]. In the targeting algorithm, the system will always try to correct latitude error through a modification of the total argument of latitude experienced during the decay trajectory and use any remaining drag controllability to correct longitude error to the extent possible. As a result, if targeting does not begin with sufficient orbit lifetime remaining, there may be some residual longitude error that the algorithm cannot correct. If control is performed only by modifying the argument of latitude of the decay trajectory, the maximum distance between any point on Earth (below the orbital inclination) and the closest reachable target location is limited. The maximum angular error will be less than the amount that Earth rotates in half an orbital period. Considering a 90 min orbital period, a given point will move 11.3deg in half an orbital period due to the rotation of the Earth. For this reason, the guidance longitude errors will not be greater than 11.3deg due to insufficient controllability, and the t-distribution is truncated at a maximum error of 11.3deg. With the normal or *t*-distributions assumed, the mean value, standard deviation (st. dev.), and degrees of freedom (d.o.f.) (for *t*-distribution) collected in Table 3, are sufficient to characterize the distributions of the aforementioned variables.

Finally, in addition to these four variables that account for the errors in the position and velocity at the DEO point, we add the uncertainty on the initial temperature of both the CubeSat structure and the D3 booms. Both temperatures are also considered normally distributed having mean values equal to the steady state temperatures and standard deviations of 10°.

3.2. High fidelity model dispersions

Even if a great effort is made to accurately model all the environmental factors affecting the dynamics, uncertainties always exist. For instance the solar activity which strongly influences the expansion/contraction of the top layers of the atmosphere cannot be predicted precisely very far in advance [35]. Therefore, we have to consider the atmospheric model, regardless of its complexity and accuracy, with some degree of uncertainty. For a full characterization of the flow field, we need to know the upstream state variables: density ρ_∞, temperature T_∞, and pressure P_∞. As suggested in Ref. [3], a uniform distribution can be used to model the uncertain density within ± 20% the value provided by the selected atmospheric model. This choice is due to the high entropy of the uniform distribution, making it the most conservative approximation when limited other modeling information is available [31]. We use the same characterization for T_∞ and P_∞ as well. In addition, we consider uncertainties on the dynamic viscosity μ_∞ and the free stream velocity magnitude V_∞. The former includes the uncertainties in the Sutherland law [18] and is modeled by a uniform distribution within ± 20% of the expected value, while the latter takes into account the movement of the atmosphere, which especially significant for the upper layers [36]. The approximation introduced in the equations of motion, derived in Refs. [19,22], considers an atmosphere that simply follows Earth in its rotation. Thus, V_∞ is taken equal to the magnitude of the relative velocity v. To model the uncertainty on V_∞, we consider an additional random term $\hat{V}_\infty$, uniformly distributed between ± 200m/s

$$V_\infty = v + \hat{V}_\infty \tag{11}$$

Furthermore, describing the phenomena of aerodynamic and aerothermodynamic interactions between the spacecraft body and the flow field through algebraic correlations introduces approximations, simplifying assumptions, and modeling errors. To take them into account, all variables that are inputs to the correlations are considered uncertain.

In the Free molecular regime, we include the wall temperature and the Schaaf and Chambre's accommodation coefficients, σ_N, σ_T and a_c [26]. The wall temperature includes two variables: the first one for the CubeSat structure temperature T_w and the second one for the D3 booms temperature T_w^{D3B}. They are uniformly distributed within ± 50% with respect to the value provided by the integration of the thermal equations [19]. Accommodation coefficients are considered for the interaction of both the CubeSat structure material (Aluminum) with air, σ_N^{Al}, σ_T^{Al} and a_c^{Al}, and the D3 booms material (stainless steel) with air, σ_N^{ss}, σ_T^{ss} and a_c^{ss}. They are modeled as normally distributed with the parameters reported in Table 3.

In the Transition regime, the Free molecular-Transition and the Transition-Continuum Knudsen boundaries, Kn^{FM} and Kn^{CR}

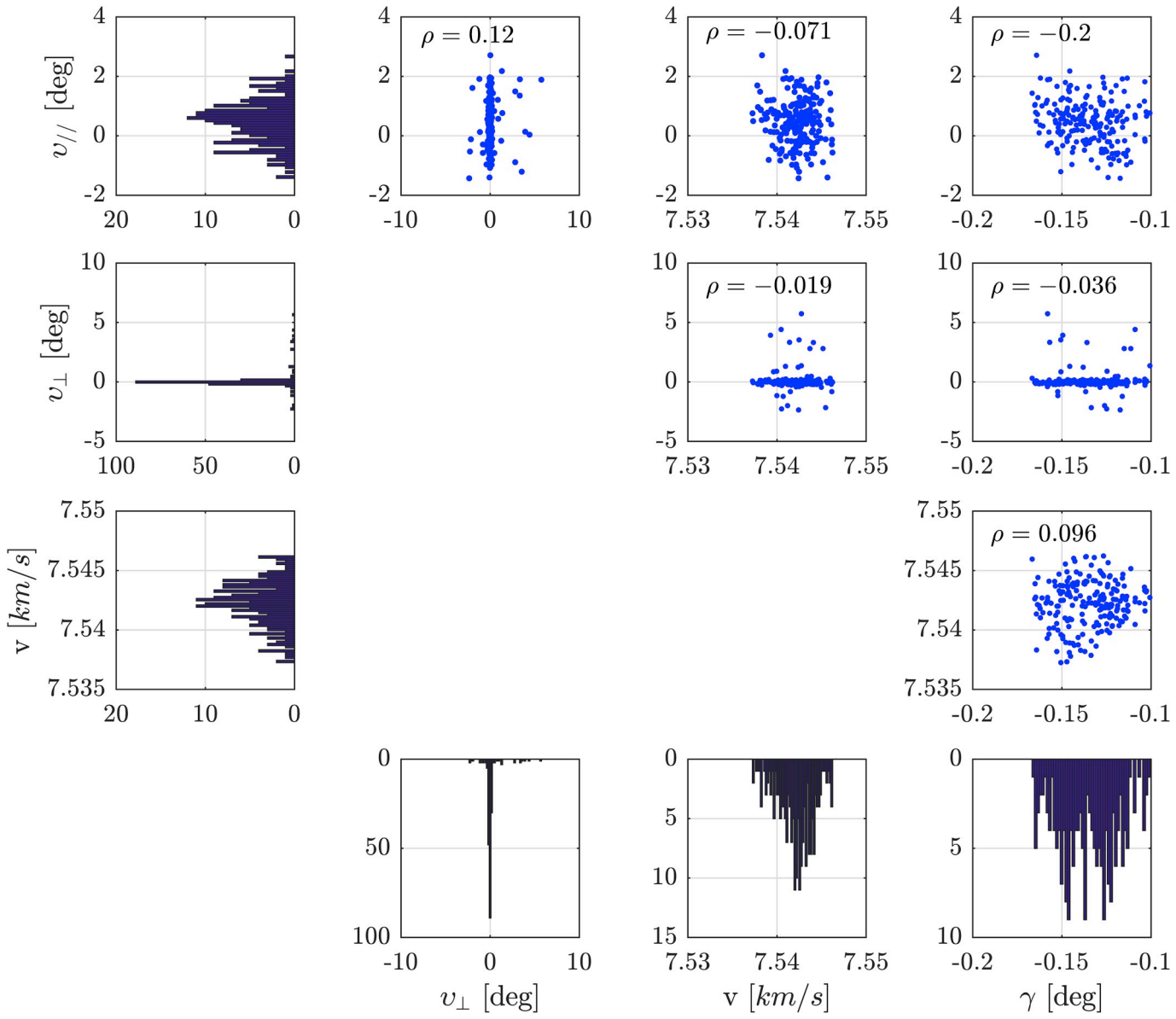

Fig. 3. Statistical distribution of GNC errors.

respectively, are regarded as random variables and are used both in the Wilmoth's and in the Legge's bridging formulas [24,37]. Their logarithms are normally distributed with mean values equal to the limits suggested by Wilmoth et al. in Ref. [37]: 1 for the Free molecular-Transition boundary and -2 for the Transition-Continuum boundary. The standard deviations are taken equal to 0.33 so that the three-sigma errors differ from the suggested values by one order of magnitude.

In the Continuum regime, we distinguish between blunt and sharp nosed objects. A blunt nose is considered when the D3 booms have not yet melted and provide attitude stabilization in face pointing mode. In this case, we include in the list of uncertainties all the thermodynamic variables of interest (Lewis number, density, pressure, specific enthalpy, dynamic viscosity, velocity gradient, and dissociation enthalpy) both at the edge of the boundary layer of the stagnation point (indicated with the subscript $t2$ in Ref. [19]) and at the wall, that appear in the Fay and Riddel's correlation [28] and in the Modified Newton Law [27]. All the selected statistical characteristics are provided in Table 3. To compute the average heat power on the different faces of the CubeSat from the estimated stagnation heat, the Koppenwallner's formula is utilized [8]. An uncertain coefficient κ_{Kopp} is considered in this formula to account for the error in the percentage of stagnation heat ($\dot{q}_s$) that reaches the other surfaces ($\dot{q}_{w_i}$), making the final formula as:

$$\dot{q}_{w_i} = \dot{q}_s[\kappa_{Kopp} + (1 - \kappa_{Kopp})\sin\theta_i] \tag{12}$$

θ_i is the inclination angle between the i-th surface and the freestream: $\theta_i = \arccos(\hat{\mathbf{n}}_i \cdot \hat{\mathbf{V}}_\infty) - \pi/2$. κ_{Kopp} is normally distributed with a mean of 0.1 as prescribed by the Koppenwallner's formula and 0.02 as the standard deviation. The sharp nose model is used for both the edge and the corner pointing modes, which are necessary to characterize the tumbling mode of the spacecraft after the D3 booms melt. In light of this, we have to consider the Eckert solution [29] and Newton law [17] for sharp nosed objects (see Table 1). Using the Eckert solution adds to the list of uncertainties all the thermodynamic variables of interest (Prandtl number, density, dynamic viscosity, velocity magnitude and specific enthalpy) both at the reference condition (indicated with superscript *) and at the edge of the boundary layer (indicated with subscript e). In addition, the pressure coefficient given by the Newton law can be modified to account for uncertainties as:

$$c_{P_i} = \kappa_{Newt} \sin^2\theta_i \tag{13}$$

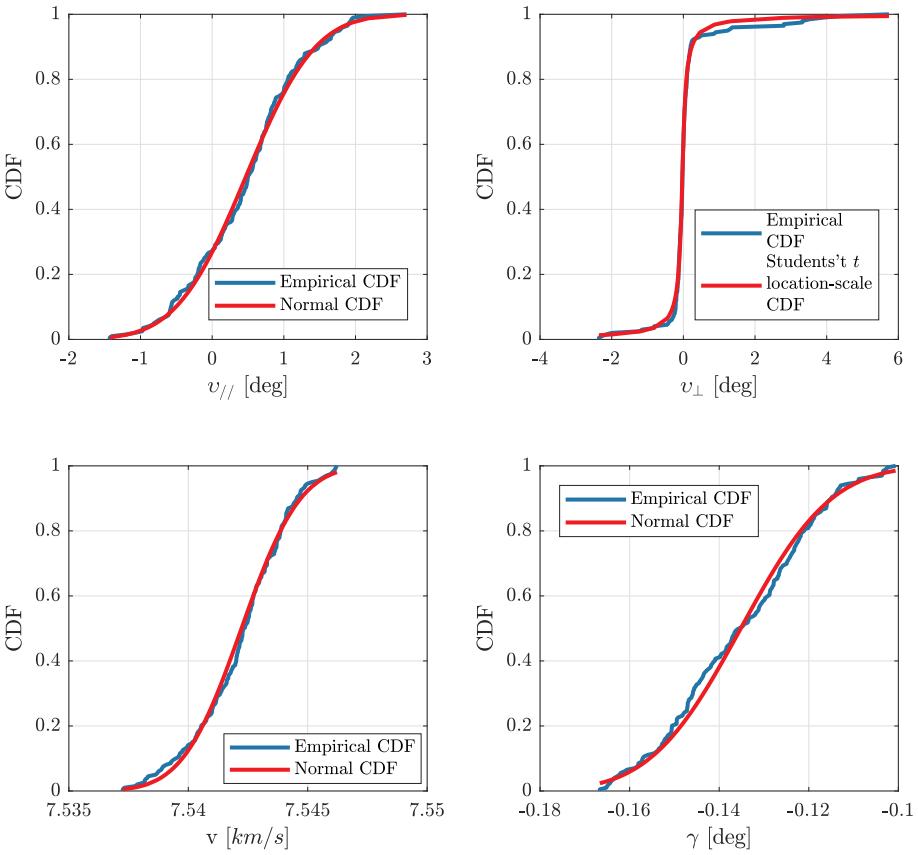

Fig. 4. Comparing of CDF resulting from the statistical fitting of the GNC errors.

where κ_{Newt} is a normally distributed random variable with a mean value of two as prescribed by the Newton's law itself and 0.2 as standard deviation. When the D3 booms bend before melting, the Li and Nagamatsu theory is introduced to estimate the drag produced by the booms [38]. This approximated model takes as inputs most of the thermodynamic variables introduced so far, with the addition of the temperature at the stagnation point T_{t2}, which must also be added to the list of uncertainties.

The contribution to the heat power due to radiation with the air flow is estimated with the Hamilton correlation [39]. An additional multiplying coefficient κ_{Ham} is added here to include some uncertainty in this correlation and is uniformly distributed between ± 50%. In addition, part of the heat power entering into the structure by thermal exchange with the air flow is dissipated by radiation with the environment. The amount of dissipated heat over time depends on the body emissivity which we assume is not perfectly known. The emissivities are considered normally distributed with mean values of 0.18 for Aluminum and 0.38 for stainless steel with standard deviations equal to 0.02.

Another important source of uncertainty is in the fragmentation process of the spacecraft due to the severe aerothermodynamic conditions it is subjected to all along the re-entry trajectory. The demise of the spacecraft occurs when the melting temperature is reached and the thermal mass approaches zero because of the melting process. This process is very complex to predict with high accuracy. Therefore, we include here some uncertainties on the thermal model described in Ref. [19]. First, the thermal mass of the CubeSat is assumed to be the one prescribed by the model plus a uniformly distributed random variable between 0% and + 80% of the nominal thermal mass to account for some heat dispersion into the payload and into the D3 shells and motors. The thermal mass of the D3 booms is uniformly distributed between ± 20% of the nominal value. The external surface area where the heat exchange with the air flow and environment occurs may also change during the melting and fragmentation process. To account for this, the external surface area of the CubeSat structure as well as the surface areas of the D3 booms vary uniformly between ± 20% the estimated values.

After the demise of the spacecraft, we continue to follow the trajectory of a specific fragment that may survive and reach the ground. In this study case, we imagine the spacecraft is equipped with a component that can be approximated as a 300 g sphere of titanium. Its ballistic coefficient is 163 kg/m^2, normally distributed about the nominal value with 10 kg/m^2 as the standard deviation.

Finally, the spacecraft configuration and the D3 bending stiffness are not perfectly known and may change during the re-entry. Therefore, we set a normal distribution both for the inclination angle of the D3 booms and for the maximum torque they can withstand. The former has mean value of 20° with respect to the rear face of the CubeSat and 1° as the standard deviation. The latter has 0.35 Nm as the mean value and 0.0167 Nm as the standard deviation [15].

To summarize, a total of 50 uncertain variables are considered: 4 in the initial state vector given by the GNC controlled orbital decay, 2 for the initial temperature at the DEO point, 5 for the upstream flow conditions, 8 in the Free molecular regime, 2 in the Transition regime, 19 in the Continuum regime, 4 for the melting model, 2 for the radiation with the environment, 1 for the radiation with the air flow, 2 for the spacecraft configuration, and 1 for the fragment's ballistic coefficient after the spacecraft demises. All these variables and their statistical characterizations are collected in Table 3.

Table 3
Collection of all the uncertain variables in the high fidelity model.

Variable name	Symbol	Dist. type	Uniform bounds		Gaussian/Students t params		
			Left	Right	Mean	St. dev.	D.o.f.
DEO along track error	$\upsilon_{//}$	Normal	–	–	0^o	0.76^o	–
DEO cross track error[2]	$\upsilon_{\perp}$	Stud. t	–	–	0^o	0.08^o	0.95
DEO flight path angle	γ_{DEO}	Normal	–	–	-0.135^o	0.016^o	–
DEO velocity magnitude	v_{DEO}	Normal	–	–	$7.54\ km/s$	$2\ m/s$	–
DEO CubeSat temperature	T_{DEO}	Normal	–	–	$546\ K$	$10\ K$	–
DEO D3 booms temperature	$T_{\mathrm{DEO}}^{\mathrm{D3B}}$	Normal	–	–	$588\ K$	$10\ K$	–
Upstream density	ρ_{∞}	Uniform	− 20%	+ 20%	–	–	–
Upstream temperature	T_{∞}	Uniform	− 20%	+ 20%	–	–	–
Upstream pressure	P_{∞}	Uniform	− 20%	+ 20%	–	–	–
Upstream dynamic viscosity	μ_{∞}	Uniform	− 20%	+ 20%	–	–	–
Upstream velocity magnitude	$\hat{V}_{\infty}$	Uniform	$-200\ m/s$	$+200\ m/s$	–	–	–
Aluminum normal accom. coeff.	σ_N^{Al}	Normal	–	–	0.9	0.1/3	–
Aluminum tangential accom. coeff.	σ_T^{Al}	Normal	–	–	0.9	0.1/3	–
Aluminum thermal accom. coeff.	a_c^{Al}	Normal	–	–	1	0.2/3	–
Stainless steel normal accom. coeff.	σ_N^{ss}	Normal	–	–	0.9	0.1/3	–
Stainless steel tangential accom. coeff.	σ_T^{ss}	Normal	–	–	0.9	0.1/3	–
Stainless steel thermal accom. coeff.	a_c^{ss}	Normal	–	–	1	0.2/3	–
CubeSat wall temperature	T_w	Uniform	− 50%	+ 50%	–	–	–
D3 booms wall temperature	T_w^{D3B}	Uniform	− 50%	+ 50%	–	–	–
Logarithm of Free molecular-Transition Knudsen boundary	$\log_{10}Kn^{\mathrm{FM}}$	Normal	–	–	1	1/3	–
Logarithm of Continuum-Transition Knudsen boundary	$\log_{10}Kn^{\mathrm{CR}}$	Normal	–	–	− 2	1/3	–
Density at the wall	$\rho_{w,t}$	Uniform	− 20%	+ 20%	–	–	–
Dynamic viscosity at the wall	$\mu_{w,t}$	Uniform	− 20%	+ 20%	–	–	–
Enthalpy at the wall	$h_{w,t}$	Uniform	− 20%	+ 20%	–	–	–
Prandtl number at the wall	$Pr_{w,t}$	Uniform	− 20%	+ 20%	–	–	–
Stagnation density	ρ_{t2}	Uniform	− 20%	+ 20%	–	–	–
Stagnation dynamic viscosity	μ_{t2}	Uniform	− 20%	+ 20%	–	–	–
Velocity gradient at stagnation point	$\left(\frac{\mathrm{d}u_e}{\mathrm{d}x}\right)_{t2}$	Uniform	− 50%	+ 50%	–	–	–
Stagnation pressure	P_{t2}	Uniform	− 20%	+ 20%	–	–	–
Stagnation temperature	T_{t2}	Uniform	− 20%	+ 20%	–	–	–
Lewis number	Le	Uniform	1	1.4	–	–	–
Dissociation enthalpy	h_D	Uniform	− 20%	+ 20%	–	–	–
Reference Prantl number	Pr^*	Uniform	− 20%	+ 20%	–	–	–
Reference density	ρ^*	Uniform	− 20%	+ 20%	–	–	–
Reference dynamic viscosity	μ^*	Uniform	− 20%	+ 20%	–	–	–
Velocity at the edge of the boundary layer	v_e	Uniform	− 20%	+ 20%	–	–	–
Recovery enthalpy	h_r	Uniform	− 20%	+ 20%	–	–	–
Enthalpy at the wall	h_w	Uniform	− 20%	+ 20%	–	–	–
Koppenwallner's formula coefficient	κ_{Kopp}	Normal	–	–	0.1	0.02	–
Newton's formula coefficient	κ_{Newt}	Normal	–	–	2	0.2	–
Hamilton's correlation coefficient	κ_{Ham}	Uniform	− 50%	+ 50%	–	–	–
CubeSat thermal mass	m_{th}	Uniform	+ 0%	+ 80%	–	–	–
D3 booms thermal mass	m_{th}^{D3B}	Uniform	− 20%	+ 20%	–	–	–
CubeSat external surface	S_{ext}	Uniform	− 20%	+ 20%	–	–	–
D3 booms external surface	S_{ext}^{D3B}	Uniform	− 20%	+ 20%	–	–	–
CubeSat emissivity	ε^{Al}	Normal	–	–	0.18	0.02	–
D3 booms emissivity	ε^{ss}	Normal	–	–	0.38	0.02	–
D3 booms deflection angle	α^{D3B}	Normal	–	–	20^o	1^o	–
D3 booms maximum bending torque	C^{Max}	Normal	–	–	$0.35\ Nm$	$0.05/3\ Nm$	–
Fragment ballistic coefficient	β_{Frag}	Normal	–	–	$163\ kg/m^2$	$10\ kg/m^2$	–

4. Reduced order model of the re-entry

4.1. Purpose

The large number of uncertain variables in the high fidelity model may strongly hinder the estimation of low probabilities, especially when a reliability based approach [31] such as the Inputs' Statistics method is employed. This issue is known in the literature as the *Curse of dimensionality* [40]. In this section, we describe a computationally efficient reduced order model that is able to capture the effects of the high fidelity model using a smaller number of specially selected variables, named hereafter “high level” variables.

For instance, the ballistic coefficient is a very useful parameter because it entirely includes the effects of the variation in time of both the drag coefficient and the spacecraft mass. Another example is the demise altitude of the spacecraft. It is the conclusive event of a progressive process, caused firstly by the temperature increase due to the thermal exchange with the flow and then by the decrease of the thermal mass of the spacecraft when the temperature reaches the melting point. Hence, if the demise altitude and the ballistic coefficient were known a priori, the computation of the drag coefficient and convective heat power into the structure would not be necessary. In other words, the aerodynamic

and the aerothermodynamic models would not be necessary at all. Since they include most of the uncertainties of the problem, we can strongly reduce their number. In addition, the aero- and the aero-thermo-dynamic models usually require the majority of the time when numerically propagating a re-entry trajectory. Therefore, the reduced order model has two important advantages: 1) it decreases the number of uncertain variables and 2) it significantly speeds up the entire simulation. The selected high level variables are statistically characterized by a MC simulation of the high fidelity model. Since in this case we are not interested in a low probability estimate but rather on the overall description of their distribution, the number of MC samples can be limited to few thousands.

4.2. Description

The reduced order model contains the same dynamic model as the high fidelity model, but includes the kinematic and dynamic equations only [19]. They are written in the scalar form given by Vihn et al. in Ref. [22]. They consider the spacecraft as a point mass having three translational degrees of freedom and are used to integrate position and velocity of the spacecraft in time. The 2001 United States Naval Research Laboratory Mass Spectrometer and Incoherent Scatter Radar Exosphere model (NRLMSISE-00) [41] is chosen as most appropriate atmospheric model. The effect of the second zonal harmonic J_2 is accounted for in the gravitational force model using the procedure given by Vallado in Ref. [42]. Therefore, to propagate the re-entry dynamics, we need to know i) the variation of the ballistic coefficient in time and ii) when the ballistic coefficient abruptly changes. With the ballistic coefficient (β) known, we can express the acceleration due to the aerodynamic drag as:

$$\mathbf{D} = -\frac{1}{2\beta}\rho_\infty V_\infty^2 \mathbf{j}'' \tag{14}$$

where the upstream density ρ_∞ is given by the atmospheric model and the freestream velocity V_∞ is approximated as the vehicle velocity with respect to Earth v. $\mathbf{j}''$ is the second unit vector of the VCI reference frame [19]. In a typical simulation of the high fidelity model, we can recognize two main events which induce a nearly instantaneous variation of the ballistic coefficient: 1) the bending of the D3 booms or their total demise and 2) the spacecraft demise.

Therefore, as illustrated in Fig. 5, we can divide the entire simulation into four parts:

1. altitude higher than 120 km, where the ballistic coefficient is approximately constant and equal to that of the spacecraft at the DEO point β_{DEO};

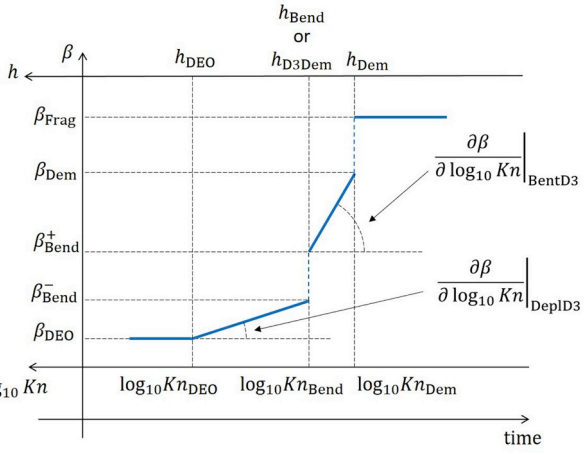

Fig. 5. Piecewise linear approximation of the ballistic coefficient in the reduced order model.

2. from 120 km down until the bending altitude h_{Bend} or the D3 booms' demise altitude h_{D3Dem}, where the ballistic coefficient is considered linearly varying with the logarithm of the Knudsen number. The initial value is β_{DEO} and the slope is computed as:

$$\left.\frac{\partial\beta}{\partial \log_{10} Kn}\right|_{\mathrm{DeplD3}} = \frac{\beta^-_{\mathrm{Bend}} - \beta_{\mathrm{DEO}}}{\log_{10}(Kn_{\mathrm{Bend}}/Kn_{\mathrm{DEO}})} \tag{15}$$

where β^-_{Bend} is the ballistic coefficient immediately before the bending of the booms or their demise and Kn_{Bend} is the corresponding Knudsen number.

3. From the bending/demise altitude of the D3 booms down until the spacecraft demise altitude h_{Dem}, where the ballistic coefficient is again considered linearly varying with the logarithm of the Knudsen number. The initial value is β^+_{Bend}, i.e. immediately after the bending or the demise of the booms, and the slope is computed as:

$$\left.\frac{\partial\beta}{\partial \log_{10} Kn}\right|_{\mathrm{BentD3}} = \frac{\beta_{\mathrm{Dem}} - \beta^+_{\mathrm{Bend}}}{\log_{10}(Kn_{\mathrm{Dem}}/Kn_{\mathrm{Bend}})} \tag{16}$$

where β_{Dem} is the ballistic coefficient of the spacecraft just before the CubeSat structure demises and Kn_{Dem} is the corresponding Knudsen number.

4. From the spacecraft demise altitude down until ground impact, where the ballistic coefficient is considered constant and equal to the fragment ballistic coefficient β_{Frag}

With this piecewise linear approximation, only 7 high level variables are necessary for the full description of the ballistic coefficient all along the re-entry propagation: β_{DEO}, $(\partial\beta/\partial \log_{10}Kn)_{\mathrm{DeplD3}}$, h_{Bend}, β^+_{Bend}, $(\partial\beta/\partial \log_{10}Kn)_{\mathrm{BentD3}}$, h_{Dem}, β_{Frag}. In order to complete the description of the reduced order model, the uncertainty on the atmospheric density ρ_∞ and the GNC errors at the DEO point ($v_{//}$, $v_\perp$, γ_{DEO} and ν_{DEO}) must be added. Thus, the number of uncertain variables is decreased from 50 in the high fidelity model to 12 high level variables in the reduced order model. This strongly reduces the curse of dimensionality issue of the Inputs' Statistics method [43] and decreases the computational time for the propagation of a single re-entry trajectory by approximately an order of magnitude. On the same standard desktop computer, approximately 30 s were required by the high fidelity model compared to about 0.7 s when the trajectories were evaluated using the reduced order model.

4.3. Statistical characterization

Because the assumption of normality does not hold (except for the GNC errors) and because the variables are generally correlated, the statistical characterization of the reduced order model is computationally expensive compared to a model where the variables are normally distributed and uncorrelated. As a consequence, the minimum number of MC runs to guarantee a predetermined confidence level and relative error for a given variable has to be estimated through the more general approach given by Rubino and Tuffin in Ref. [44]. The standard MC estimator of the probability that the variable exceeds a given threshold is a binomial random variable. Thus, the confidence level on this probability estimator $\hat{\gamma}$ is given by:

$$z_{\alpha/2}\frac{\sqrt{\gamma(1-\gamma)}}{\sqrt{N}} \le \hat{\gamma} \le z_{1-\alpha/2}\frac{\sqrt{\gamma(1-\gamma)}}{\sqrt{N}} \tag{17}$$

where N is the number of samples, $1-\alpha$ is the confidence level we want to achieve, γ is probability that has to be estimated, and $z_{1-\alpha/2}$ is the $(1-\alpha/2)$-quantile of the standard normal distribution. Setting the half-width of the confidence level equal to the desired relative error RE and solving eq. (17) for N, the minimum required number of runs is

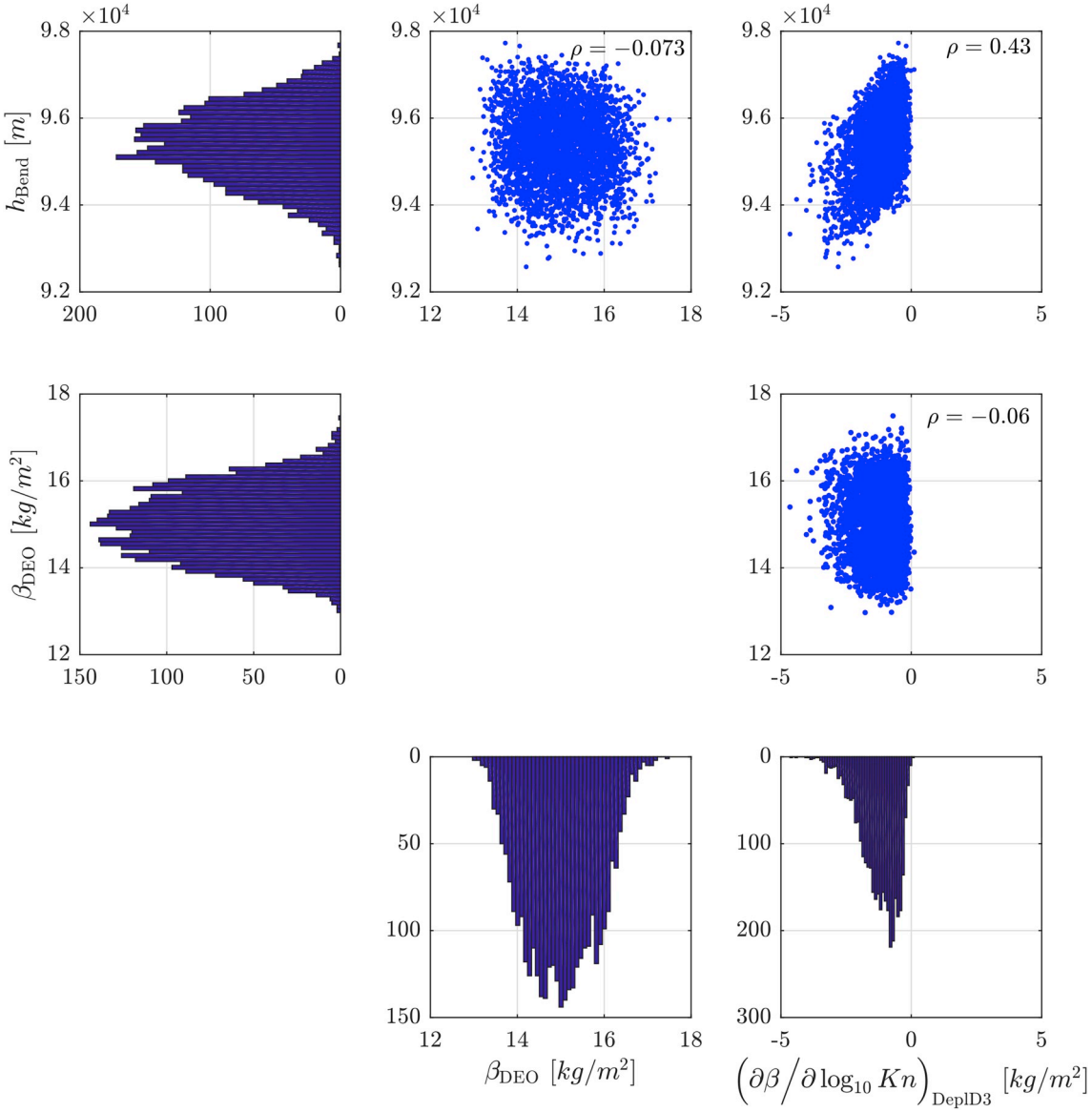

Fig. 6. Distributions of the ballistic coefficient at the DEO point, the slope of the ballistic coefficient with deployed D3 booms, and the D3 bending (or D3 demise) altitude.

computed as:

$$N = \frac{z^2_{1-\alpha/2}}{RE^2}\frac{1-\gamma}{\gamma} \tag{18}$$

In order to have a good overall statistical description of the aforementioned variables, we impose 95% confidence level and 10% relative error on at least 10% probability estimate, which requires running 3460 samples of the high fidelity model. Considering 30 s as the average time required for the propagation of a single re-entry trajectory, the necessary time to statistically characterize the reduced order model is on the order of 30 h. This time is however extremely small compared to the one necessary if the high fidelity model is used to attempt to compute directly the extremely low probabilities associated with the safety boxes (about 2% of the time for a 99.99% safety box). The MC analysis has been performed considering the 0deg latitude, 99deg longitude, and 120km geodetic altitude DEO point introduced in section 3.1. Examples of numerical distributions of some of the high level variables are given in Fig. 6.

Analysing these distributions, we note that β_{DEO}, h_{Bend}, and h_{Dem} closely follow a normal distribution, as confirmed by the Kolmogrov-Smirnov test [32]. $(\partial\beta/\partial \log_{10} Kn)_{\mathrm{DeplD3}}$ can be approximate as a Gamma distribution [45]. β^+_{Bend} and $(\partial\beta/\partial \log_{10} Kn)_{\mathrm{BentD3}}$ have more complex distributions because these variables incorporate the characteristics of the ballistic coefficients when the D3 booms bend and when they demise. Since in the second case the CubeSat keeps falling in a tumbling mode without the D3, the ballistic coefficient is higher and increases faster than the case where the D3 booms are still attached but bent. Having the booms demise before bending, however, is quite unlikely since it occurs on average during only about 4% of the simulations. To model these two distributions, a non parametric Gaussian kernel distribution is suggested [31,46] and justified again with the Kolmogrov-Smirnov test. All the parameters of the marginal distributions are collected in Table 4. The correlation among the variables is modeled through a Gaussian copula [31,47], but it is considered only when it is significant. In particular, correlations are considered between h_{Dem} and β^+_{Bend}, between $(\partial\beta/\partial \log_{10} Kn)_{\mathrm{BentD3}}$ and h_{Bend}, between ρ_∞ and h_{Bend} or h_{Dem}, and between β^+_{Bend} and $(\partial\beta/\partial \log_{10} Kn)_{\mathrm{BentD3}}$.

The final impact point predicted by the reduced order model is

Table 4
Statistical characterization of the high level variables necessary to describe the profile of the ballistic coefficient in the reduced order model.

Variable name	Symbol	Dist. type	Gaussian params		Gamma params	
			Mean	St. dev.	a	b
Ballistic coefficient at DEO point	β_{DEO}	Normal	15 kg/m^2	0.79 kg/m^2	–	–
Slope of the ballistic before D3 bending or demise	$\left(\frac{\partial\beta}{\partial\log_{10}Kn}\right)_{\text{DeplD3}}$	Gamma	–	–	4.19	0.346 kg/m^2
D3 bending geodetic altitude	h_{Bend}	Normal	95.4 km	850 m	–	–
Ballistic coefficient immediately after bending or demise	β^{+}_{Bend}	Non parametric	–	–	–	–
Slope of the ballistic after D3 bending or demise	$\left(\frac{\partial\beta}{\partial\log_{10}Kn}\right)_{\text{BentD3}}$	Non parametric	–	–	–	–
Demise geodetic altitude	h_{Dem}	Normal	85.9 km	208 m	–	–

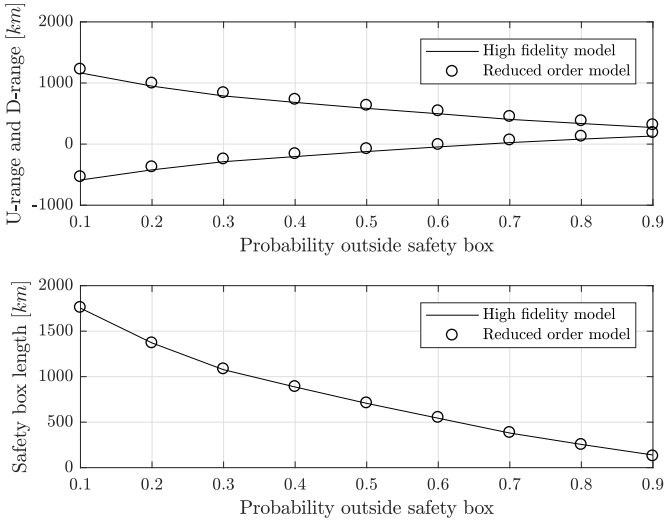

Fig. 7. Up-track range (U-range), down-track range (D-range) and full length of the safety boxes versus the associated probability computed through a MC simulation with the high fidelity and the reduced order models.

slightly different from the one predicted by the high fidelity model. This is due to both the piecewise linear approximation of the ballistic coefficient and to the fitting of the distributions of the variables and their correlations with specific distribution laws. It has been estimated that the average value of this error is on the order of 50 km in the down track direction. Nevertheless, this represents only an offset in the quantile computation, associated with a certain probability of interest. As a consequence, subtracting the mean value of the error, the quantile estimate is accurate with respect to the one predicted by the high fidelity model. Indeed, in Fig. 7, when the safety boxes dimensions, given by the up-track range (U-range) and down-track range (D-range), are plotted for different values of probability, the offset between high fidelity model and reduced order model quantiles is clearly visible (see sec. 6.1 for more details on the safety box geometry). When the total length of the safety box is computed by subtracting the U-range from the D-range, the offset is eliminated and both models have similar distributions for the total safety box length as can be confirmed by the Kolmogrov-Smirnov test.

5. International safety requirements

The risk reduction measures required for the re-entry of a spacecraft are regulated by requirements documented in Space Agencies' instructions and guidelines. The European guidelines [3] strictly follow the French Space law [48]: "*the operator responsible of a spacecraft controlled re-entry shall identify and compute the impact zones of the spacecraft and its fragments for all controlled re-entry on the Earth with a probability respectively of 99% and 99.999% taking into account the uncertainties associated to the parameters of the re-entry trajectories*".The "Safety Boxes" definition is derived from this requirement as the containment contours on the ground such that the probability that a fragment falls outside is below a controlled or known value [5,49]. This controlled value is usually called probability level and indicated by α. In particular, two safety boxes are usually of interest [3]:

- The Declared Re-entry Area (DRA) should delimit the area where the debris should be enclosed with a probability of 99% (i.e $\alpha = 10^{-2}$) given the delivery accuracy.
- The Safety Re-entry Area (SRA) should delimit the area where the debris should be enclosed with a probability of 99.999% (i.e $\alpha = 10^{-5}$) given the delivery accuracy.

The DRA is used to implement the procedures of warning and alerting the maritime and aeronautic traffic authorities. The mission operators are in fact required to provide the authorities with the technical information in order to issue NOTAM (Notice To Airmen) and AVURNAV/NAVAREA (Notice to Mariners) messages. The NOTAM area is computed as the envelop of the DRAs relative to baseline and all the back-up strategies [9]. The SRA is the indicator of a possible risk for population and properties. It used to design the re-entry trajectory such that the SRA does not extend over inhabited regions, does not impinge on State territories and territorial waters without the agreement of the relevant authorities. Usually, the re-entry trajectories are designed such that the SRA of the baseline strategy is included within the SPOUA, or South Pacific Ocean Uninhabited Area [5]. It is the largest uninhabited area on Earth, bordered by the 185 East and 275 East meridians and by the 29 South and 60 South parallels.

The NASA safety requirements [1] state that the probability of human casualty from surviving debris from a given mission must be less than 0.0001 (1:10,000) where a surviving debris object with energy greater than 15 J is considered to have a potential for casualty. For controlled re-entry, the trajectory must be designed such that surviving debris with an energy of 15 J or greater are more than 370 km from foreign landmasses and more than 50 km from US territories. In addition, the product of the probability of failure to control the re-entry location multiplied by the casualty probability from uncontrolled re-entry must be less than 0.0001. For example, a spacecraft that nominally has a 0.001 casualty probability from uncontrolled re-entry must have a 0.9 probability of successfully controlling the re-entry location. While this is the general policy, some missions may have stricter requirements. For example, if a satellite contains hazardous material such as radioactive elements that may cause harm to persons or property beyond the initial impact, or if the satellite is a member of a fleet of spacecraft, the allowable casualty probability may be less. In fact, during the European Space Agency's Automated Transfer Vehicle spacecraft mission, the permissible casualty probability from re-entry debris was only 10^{-7} [5]. In the current study, the permissible casualty probability was assumed to also be 10^{-7}.

The nominal casualty probability of the satellite assuming

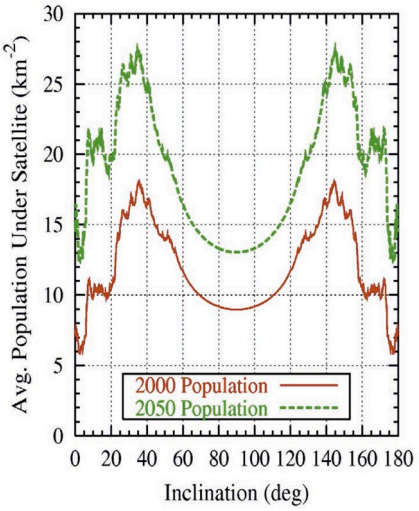

Fig. 8. Average Population Density vs. Orbit Inclination [50].

uncontrolled re-entry can be calculated based on the casualty area of the surviving orbital debris and the orbit inclination. The casualty area (D_A) in m^2 associated with the mission is given by Ref. [1] as

$$D_A = \sum_{i=1}^{N} (0.6 + \sqrt{A_i})^2 \tag{19}$$

where N is the number of debris fragments, A_i is the maximum cross sectional area of each fragment, and the factor of 0.6 m^2 accounts for the average surface area of a person that can be struck by a fragment. The total human casualty probability expectation associated with an uncontrolled re-entry is then calculated by

$$E_n = D_A P_d \tag{20}$$

where P_d represents the average population density for the given orbit. Fig. 8 from Ref. [50] gives P_d as a function of orbit inclination. In the analyzed scenario, a single debris fragment is considered that is modeled as a sphere with a radius of .025m^2. The spacecraft is in a 51.9° inclined orbit and so the estimated population density of 20/km^2 for this inclination in the year 2050 is utilized (Fig. 8). Using this value and Eq. (20) yields an expected casualty probability of $E_n = 8.3 \times 10^{-6}$ assuming an uncontrolled re-entry.

Finally, even when controlled re-entry techniques are used, the debris will land over a region on the ground, not on a specific point. The safety box concept is used in this work to estimate this region of debris landing when the re-entry control process works as expected. α is the probability of debris falling outside the safety box. If all cases where debris lands outside the box are assumed to have the same casualty risk as an uncontrolled re-entry (E_n), the casualty risk associated with the mission can be computed as:

$$E = E_n(P_f + (1 - P_f)\alpha) \tag{21}$$

where P_f is the probability of the spacecraft failing to perform a controlled re-entry (possibly due to hardware failures). Specifically, the first term $E_n P_f$ is the casualty risk associated with a potential failure of the control whereas the second term $E_n(1 - P_f)\alpha$ is the casualty risk associated with a successful controlled re-entry where debris falls outside the safety box. For eq. (21) to hold, there must be no casualty probability within the safety box. Therefore, the re-entry is designed such that the safety box is fully included within the SPOUA.

To fulfill the safety requirement, E must be lower or equal than 10^{-7}. In sec. 7, a possible approach is described to target the optimal DEO point to get the safety box fully within the SPOUA and optimize the room available. In sec. 8, the maximum allowable probability of failure P_f that still allows the mission to meet the safety requirements is computed for different DEO altitudes.

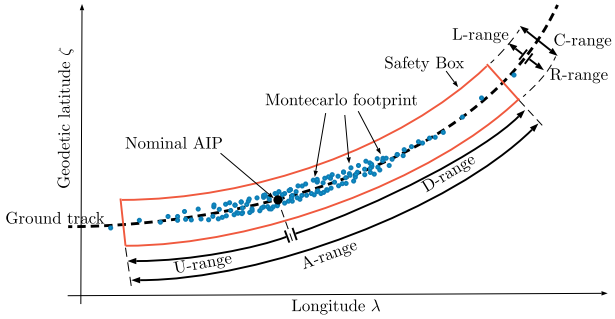

Fig. 9. Schematic representation of safety boxes geometry.

6. Safety box calculation

6.1. Safety box geometry

The safety boxes are approximated as having a rectangular shape and are usually described in terms of along track and cross track dimensions, as shown in Fig. 9. The nominal trajectory defines the ground track. The ground track is computed assuming the spacecraft continues on its orbit without perturbations. The Aimed Impact Point (AIP) is defined as a reference target and is computed by deterministically propagating the mean values of the dispersions. The along track range (A-range) is usually divided in up-track range (U-range) if the fragment falls before the AIP, and down-track range (D-range) if the fragment falls after the AIP. The sign is assumed negative if up-track and positive if down-track. They are computed as curvilinear integrations along the ground track from the AIP to the projection of the impact point over the ground track. The cross track range (C-range) is usually much smaller than the A-range and often it is simply considered constant and equal to the maximum value that it can attain as in Ref. [5]. In the D3 controlled re-entry, however, the C-range can be significant because of the heavy tail of the cross track GNC error at the DEO point, so it is more accurately estimated. When computed, the C-range can be projected on the ground track as in Fig. 9. Its sign is determined according to the second axis of a reference frame tangent to the ground track, with the first axis positive in the direction of motion and the third axis positive in the zenith direction. In other words, for an observer sitting on the ground track and aligned with the velocity vector, the C-range is positive if the fragment falls on his left (L-range) and negative if it falls on his right (R-range). The safety box associated with a given probability level is thus fully determined when the A-range and the C-range are computed.

It is important to remark on the difference between footprint and safety box concepts in order to not mix them up. The footprint is built up through a MC simulation and is the collection of all the impact points corresponding to the sample cloud. It is numerically built and a-priori it disregards any probabilistic information. Differently, the safety box is associated with a given probability level and can be derived from a statistical post-processing of the footprint. The safety box dimensions are estimated by computing the probability of a debris impact occurring outside the box itself. The smaller the probability, the larger the safety box must be.

6.2. Input-output formulation

All the variables needed to propagate the re-entry dynamics of the CubeSat equipped with the D3 device through the reduced order model have been defined in section 4 and their associated dispersion are discussed in sections 3 and 4. Therefore, the problem can be now set up with a suitable input-output formulation to apply a statistical method for the computation of the safety boxes. This formulation is schematically illustrated in Fig. 10.

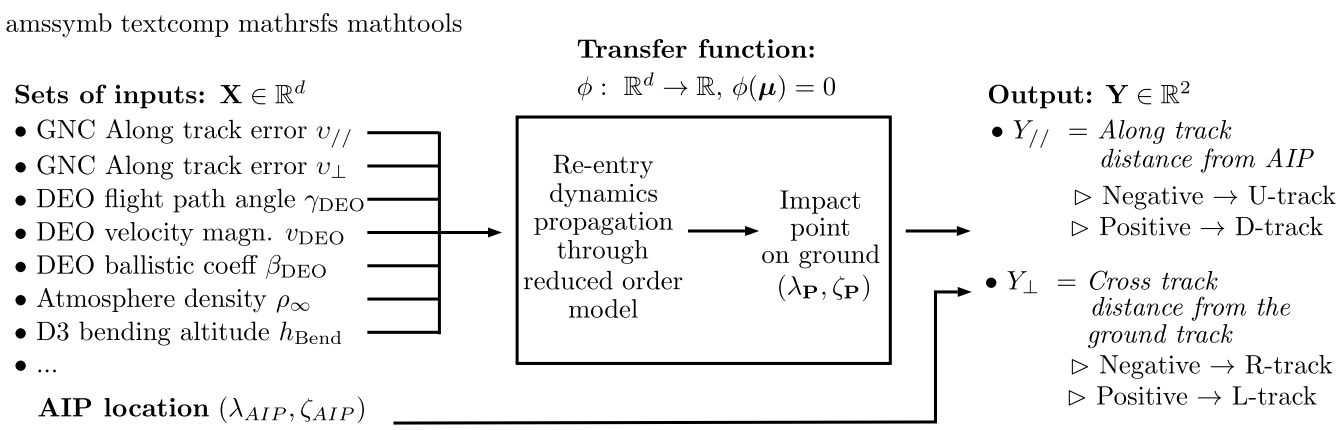

Fig. 10. Schematic illustration of the input-output formulation for the safety boxes computation.

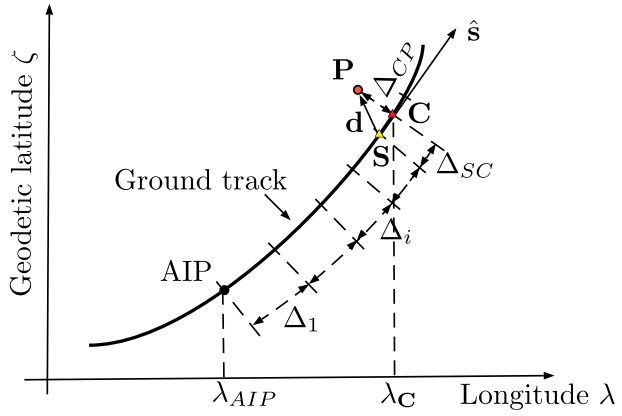

Fig. 11. Schematic illustration to clarify the computation of the along track distance of a fragment impact point with respect to the AIP.

The $d = 12$ high level variables of the reduced order model are here called inputs of the problem and are collected in the random vector $\mathbf{X} \in \mathbb{R}^d$. For any input combination, the transfer function ϕ: $\mathbb{R}^d \to \mathbb{R}^2$ propagates the re-entry dynamics up to ground impact and estimates: 1) the along track distance $Y_{//}$ with respect to the AIP and 2) the cross track distance $Y_{\perp}$ from the ground track. They are collected in the bidimensional vector $\mathbf{Y} = \{Y_{//}, Y_{\perp}\} \in \mathbb{R}^2$, called output of the transfer function. $\mathbf{Y}$ is computed in two steps:

1. project the impact point of the fragment, called **P** in Fig. 11, on the ground track as:

$$\mathbf{C} = (\mathbf{d}\cdot\hat{\mathbf{s}})\,\hat{\mathbf{s}} \tag{22}$$

where **d** joins **P** to a point on the ground track very close to it but slightly towards the AIP, which is indicated with **S**, $\hat{\mathbf{s}}$ is the unit vector tangent to the ground track in **S** oriented in the motion direction, and **C** is the projection of **P** on the ground track; computing the tangent to the ground track in **C** as:

$$\theta = \sin^{-1}(\hat{\mathbf{s}}\cdot\mathbf{j}) \tag{23}$$

2. the cross track distance is computed as

$$Y_{\perp} = \mathrm{sign}(-\sin\theta\,\mathbf{d}\cdot\mathbf{i} + \cos\theta\,\mathbf{d}\cdot\mathbf{j})\,\Delta_{CP} \tag{24}$$

whereas the along track distance can be approximated by numerically integrating the distance from the AIP as:

$$Y_{//} = \mathrm{sign}(\lambda_{\mathbf{C}} - \lambda_{AIP})\left(\Delta_{SC} + \sum_{i=1}^{n}\Delta_i\right) - Err_{RedOrdMod} \tag{25}$$

where Δ_i indicates the distance on the Earth surface between two consecutive points on the ground track, and Δ_{CS} and Δ_{CP} are the distance from **C** to **S** and from **C** to **P**, respectively. All the distances Δ_i, Δ_{CS} and Δ_{CP} are computed as the shortest distance on the ellipsoid (geodetics) given by the WGS84 model to better approximate the actual shape of Earth. This is done using the Vincenty's algorithm in Ref. [51]. The error due to the use of the reduced order model $Err_{RedOrdMod}$, estimated as 50 *km* in sec. 4, is subtracted from this integration.

6.3. Problem statement

Since the safety box is fully defined once the A-range and the C-range are defined, the problem requires the computation of four thresholds: U-range, D-range, R-range and L-range. Nevertheless, only one constraint, the required probability level α, is available so the problem admits infinite solutions. An engineering condition is therefore introduced which sets the probability outside the A-range $\alpha_{//}$ to be less than or equal to 10% of α and the probability outside the C-range $\alpha_{\perp}$ to be less than or equal to 90% of α, so that the overall probability outside the safety box is still less than or equal to α as required. This proportion was chosen because the A-range is generally much bigger than the C-range and is subject to a larger number of dispersions. It is therefore more likely that if a point falls outside the safety box and reaches an inhabited region, it will be in the along track direction. The independent $\alpha_{//}$ and $\alpha_{\perp}$ values make it possible to study the two directions separately. In both directions, the problem requires the identification of two thresholds T_1 and T_2, with $T_1 < 0$ and $T_2 > 0$, such that the probability that the output Y falls outside the interval $[T_1, T_2]$ is less than or equal to a predetermined value α:

$$1 - \mathbb{P}(T_1 \le Y \le T_2) \le \alpha \tag{26}$$

For the A-range problem T_1 will be the U-range and T_2 the D-range and $\alpha_{//}$ will be considered, while for the C-range problem T_1 will be the R-range and T_2 the L-range and $\alpha_{\perp}$ will be considered.

In addition, a sensitivity analysis on the 12 input variables has been carried on and we have found that the GNC errors on the position at the DEO point, defined in terms of along track $v_{//}$ and cross track $v_{\perp}$, do not significantly affect the A-range of the safety box. On the other hand, all the other 10 variables do not significantly affect the C-range of the safety box. This is shown in Fig. 12, where nine 4000-runs MC footprints are shown starting from three DEO points having different latitudes (0deg and ± 20deg) and a longitude of 99deg. For each DEO point, the associated MC simulations were performed considering: 1) the full set of 12 variables (green), 2) only $v_{//}$ and $v_{\perp}$ (black) and 3) the 10 variables excluding $v_{//}$ and $v_{\perp}$ (red). As can be visually verified, the black footprint accurately estimates the C-range and the red footprint matches the A-range. This is also verified with the Kolmogrov-Smirnov test and shown in Fig. 13 in terms of cumulative distribution functions for the equatorial case. Similar plots can be obtained for the other two

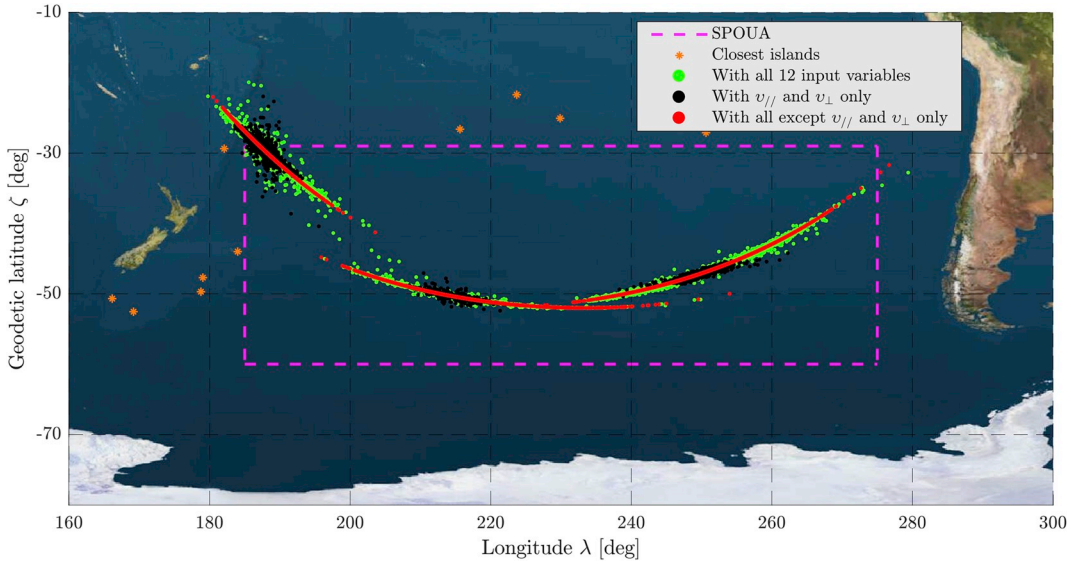

Fig. 12. Monte Carlo footprints for different DEO points and input variables.

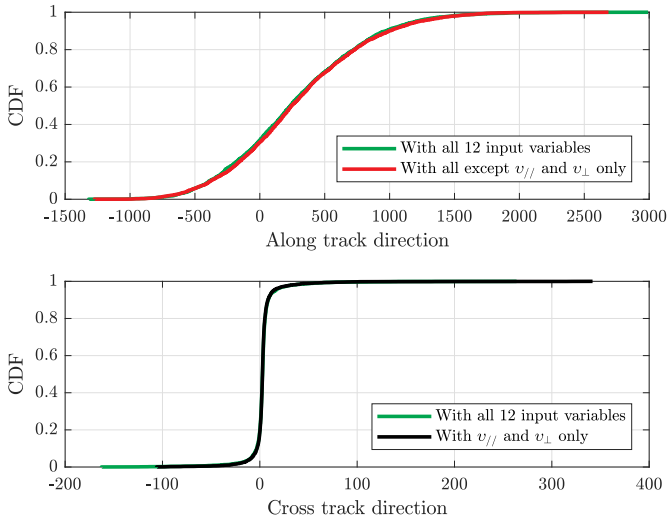

Fig. 13. CDF plot for different DEO points and input variables.

cases. Therefore, this subdivision of 10 + 2 input variables is assumed to always be valid for this problem and is adopted in all the following safety box computations. This is beneficial when the Inputs' Statistics method is applied because it further reduces the problem dimensionality.

6.4. Inputs' statistics method

When the Inputs' Statistics method is chosen, the problem is formulated in an alternative way with respect to eq. (26). Instead of working on the output distribution, the objective is to approximate the optimal failure domain Ω_f^{Opt} of problem [43]. Ω_f^{Opt} corresponds to the failure domain which provides the smallest possible interval $[T_1, T_2]$ and in the current problem, results in the smallest possible safety box. The Single Step Inputs' Statistics method attempts to find Ω_f^{Opt} by considering the d-dimensional contour surfaces $\tilde{\varepsilon}$ of the multivariate probability density function (pdf) f of the input vector $\mathbf{X}$. The particular $\tilde{\varepsilon}$ enclosing a probability equal to $1-\alpha$ is chosen and the two thresholds $\tilde{T}_1$ and $\tilde{T}_2$ are computed as the minimum and maximum cases which may occur inside $\tilde{\varepsilon}$ [49]. This initial approximation is always conservative and may be quite accurate when few input dimensions are considered. This is the case for the computation of the C-range of the safety box because only two input variables are used. For that reason, the Single Step solution of the C-range is retained as final one in all the following results. On the other hand, since 10 input variables are considered for the A-range problem, the Single Step approximation is too conservative and so we rely on the Multistep algorithm [43]. The Multistep algorithm improves the Single Step solution by iteratively estimating the error on the probability estimate through a Crude Monte Carlo (CMC) method [31]. The CMC method works by simulating trajectories with initial conditions selected outside the current $\tilde{\varepsilon}^k$ to reduce the dimension of the successive $\tilde{\varepsilon}^{k+1}$ input domains. This ultimately brings the current failure domain $\tilde{\Omega}_f$ closer and closer to the optimal one Ω_f^{Opt}. The details of the Multistep algorithm can be found in Ref. [43], and a more in-depth treatise on the Inputs' Statistics method is contained in Ref. [52].

As described so far, the Inputs' Statistics method is based on the d-dimensional pdf and its contours surfaces. Therefore, as long as the marginal distributions of the input variables are known and the correlation is somehow defined, the Inputs' Statistics method can be applied to the problem. This is the case for the problem under analysis here because the marginals have been defined in sec.3.1 and in sec.4, and a Gaussian copula is used to take into account the correlation among the variables. However, there are two approaches to the Inputs' Statistics method. The first is to directly use the contour surfaces of the pdf in the physical space. This approach may be of interest if the multivariate pdf and its contours can be mathematically described in an easy manner. Otherwise, a better approach is to transform the physical space into the standard normal space such that the contour surfaces are d-dimensional spheres centred on the origin of the axes and described as:

$$\varepsilon(t) = \{\mathbf{x} \in \mathbb{R}^d : \mathbf{x}^T\mathbf{x} \leq t\} \tag{27}$$

where t is the sphere radius squared. We adopt the second approach in this work because the marginals follow different types of distributions (normal, gamma, uniform, kernel approximated, etc.) and so the mathematical description of the multivariate pdf is not known. This transformation is achieved through the Diagonal transformation [31] (particular case of the Probability Integral transform [53]) for variables that are not correlated and the Nataf transformation [54,55] for the correlated variables. More specifically, if F_{X_i} is the marginal cumulative distribution function (cdf) of the i-th physical variable x_i, the Diagonal transformation τ_D states that:

$$u_i = \tau_D(x_i) = \Phi_{0,1}^{-1}\left(F_{X_i}(x_i)\right) \tag{28}$$

is a standard normal variable, i.e. with zero mean and unitary standard

Table 5
Summary of results and Inputs' Statistics performances for the computation of A-ranges and C-ranges for safety boxes associated with different levels of probability. Dimensions are given in kilometers.

Prob.α	A-range					C-range			
	$\alpha_{//}$	N	$\frac{N^{MIS}}{N}\%$	U-range	D-range	$\alpha_{\perp}$	R-range	L-range	Error%
10^{-1}	10^{-2}	3.8×10^4	80%	− 910	1780	9×10^{-2}	− 20	32	+ 190%
10^{-2}	10^{-3}	3.8×10^5	41%	− 1150	2330	9×10^{-3}	− 57	144	+ 95%
10^{-3}	10^{-4}	3.8×10^6	15%	− 1330	2810	9×10^{-4}	− 76	190	+ 20%
10^{-4}	10^{-5}	3.8×10^7	4%	− 1480	3300	9×10^{-5}	− 91	202	+ 9%

deviation. $\Phi_{0,1}^{-1} = \sqrt{2}\,\mathrm{erf}^{-1}(2x-1)$ is the inverse of the standard normal cdf. For the Inputs' Statistics method, we are mostly interested in the inverse transformation τ_D^{-1}, because the search points of the optimization algorithm have to be converted to the physical space in order to compute the cost function ([49]). The inverse transformation can be written as:

$$x_i = F_{X_i}^{-1}(\Phi_{0,1}(u_i)) \tag{29}$$

where $F_{X_i}^{-1}$ is the inverse of the i-th marginal cdf. The Nataf transformation τ_N is the composition of two successive transformations: $\tau_N = \tau_{N_1} \circ \tau_{N_2}$. The first one coincides with the Diagonal transformation: $\tau_{N_1} \equiv \tau_D$, converting the physical vector $\mathbf{X}$ with correlation matrix $\mathbf{R}$ into a Gaussian vector $\mathbf{Z}$ with correlation matrix $\mathbf{R}_0$ and with standard normal marginal distributions (generally $\mathbf{R} \neq \mathbf{R}_0$). The second transformation τ_{N_2} converts $\mathbf{Z}$ into the standard normal vector $\mathbf{U}$ with the independent components as:

$$\mathbf{U} = \tau_{N_2}(\mathbf{Z}) = \mathbf{\Gamma}\,\mathbf{Z} \tag{30}$$

where $\mathbf{\Gamma}$ is any square root of $\mathbf{R}_0^{-1}$. A common choice of $\mathbf{\Gamma}$ is the Cholesky decomposition [56] of $\mathbf{R}_0^{-1}$. In the simple case of Gaussian copula, $\mathbf{R}_0$ coincides with the correlation matrix of $\mathbf{Z}$, so the entire transformation τ_N is defined and its inversion is straightforward.

6.5. Some typical results

Starting the re-entry propagation from the 120 km DEO point introduced in sec.3.1, we tested the algorithm on several required safety box probabilities. The results as well as the associated performances of the Inputs' Statistics method are collected in Table 5. The plot of the associated safety boxes are given in Fig. 14. As expected, for the A-range computation, the efficiency of the Multistep Inputs' Statistics with respect to the CMC method increases with a decrease of the allowable probability of debris landing outside the safety box. For $\alpha_{//} = 10^{-4}$ and $\alpha_{//} = 10^{-5}$ the method performs well, requiring only 15% and 4% of the samples used by the CMC. The convergence analysis for the A-range corresponding to $\alpha_{//} = 10^{-4}$ is given in Fig. 15 and similar convergence results were obtained for all the other probability levels. The number of iterations is, in all the cases, lower than 30. The computational time is almost proportional to the number of propagated samples if the time for the optimization processes is neglected. Thus the same efficiency ratio holds also for the computational time. Considering an average of 0.7 s for a single run of the reduced order model, the time required to estimate $\alpha_{//} = 10^{-5}$ with the Inputs' Statistics method is 12 days. Using instead the CMC, $N = 3.8 \times 10^7$ propagations are required to achieve the 95% CL and 10% RE, so the computation would last 10 months. If to this we add the time required to statistically characterize the variables of the reduced order model, the time can be compared with a hypothetical CMC applied directly to the high fidelity model. We used 3460 runs of the high fidelity model (average time of 30 s). So the total time for the Inputs' Statistics with the reduced order model is 13.5 days. The total time of CMC with the high fidelity model would be 36 years.

These orders of magnitude of computing time reduction justify the use of the Inputs' Statistics method coupled with the reduced order model for the computation of very small probabilities. The computational time was further reduced by implementing a parallel computation on a desktop computer equipped with a four-core processor. We can also note that the A-range increases linearly with the decrease of the logarithm of the probability. With a total probability of $\alpha = 10^{-4}$, the A-range length is 4780 km, so we can still easily fit the safety box within the SPOUA.

The C-range computation is instead performed with the Single Step algorithm. The computational time is almost negligible since only a few minutes are necessary to perform the two optimization processes. To estimate the accuracy of the Single Step solution, the Multistep algorithm has been applied to the C-range problem and the error between the two solutions is computed as:

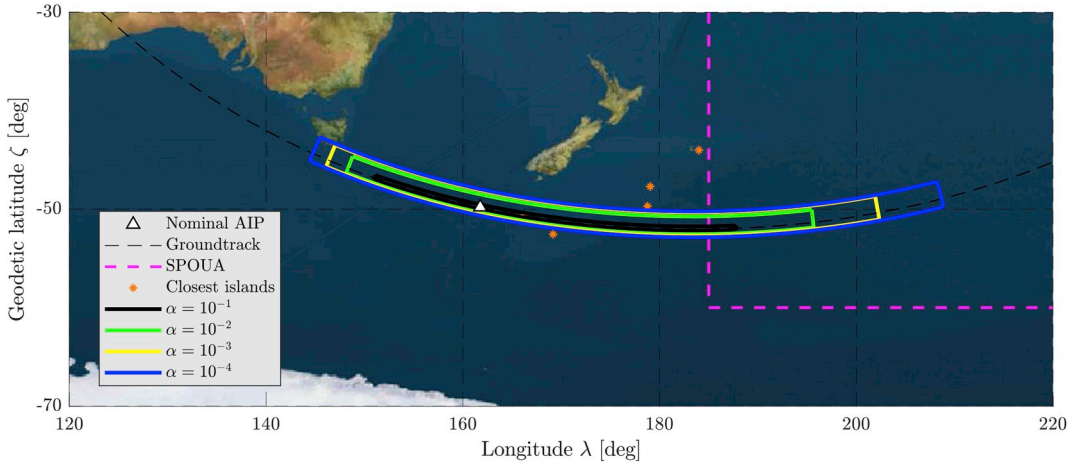

Fig. 14. Safety boxes for different probability levels associated with DEO point 99deg longitude, 0deg latitude and 120 km geodetic altitude.

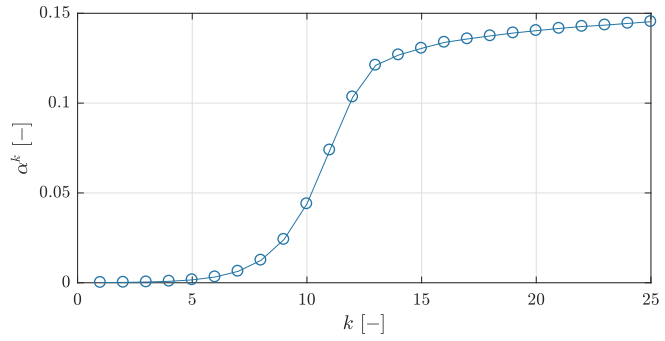

(a) Increase of the probability outside ellipsoid $\widetilde{\mathcal{E}}^k$.

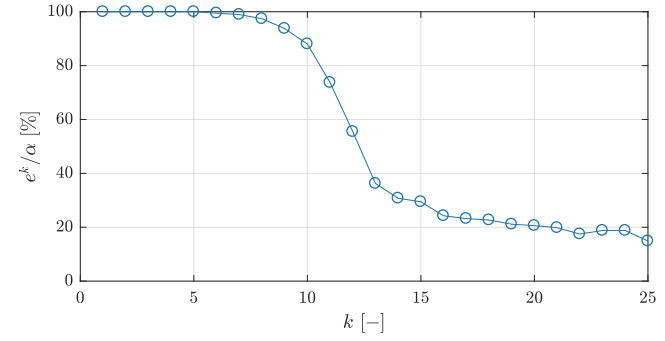

(b) Decrease of the error in percentage w.r.t. α.

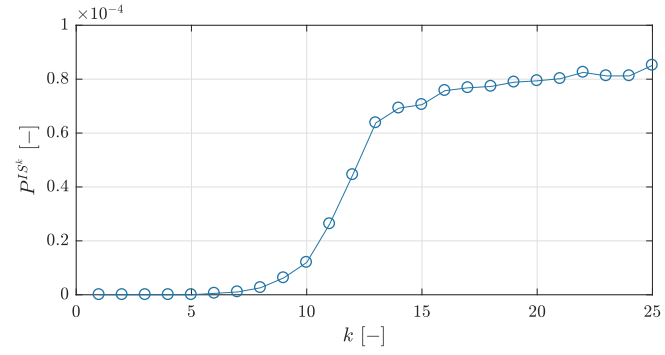

(c) Convergence of the probability to α.

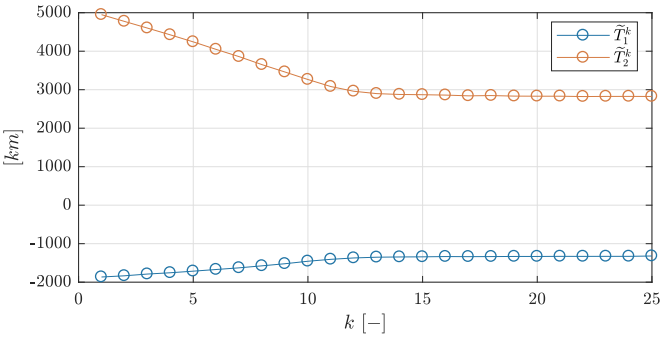

(d) A-range interval decrease.

Fig. 15. Convergence analysis for a the A-range corresponding to $\alpha_{//} = 10^{-4}$. Starting with $N = 3.8 \times 10^6$ to have 95% CL and 10% RE.

$$\text{Error}_{\%} = 100\left(\frac{\text{C-range}^{SingleStep}}{\text{C-range}^{Multistep}} - 1\right) \tag{31}$$

As shown in Table 5, this error is always positive because the Single Step solution is always conservative. The error decreases logarithmically with a logarithmic decrease of the required probability. For $\alpha_{\perp} = 9 \times 10^{-5}$ the Single Step solution is only 9% larger than the Multistep solution, so for low probability levels the Multistep algorithm is not necessary. Furthermore, the C-range is always quite small (about 6 %− 7% of the A-range), so the A-range is definitely the primary parameter to be adjusted to ensure the safety box lies inside the SPOUA.

7. Optimal de-orbit point

7.1. Purpose

In the previous section, the procedure to compute the safety box associated with a general probability level when starting the re-entry propagation from a specific DEO point has been described. Here, we explain how to generalize the statistical characterization of the input variables in order to be able to change the DEO point and directly re-apply the Inputs' Statistics method to compute the new associated safety boxes without re-run the MC analysis with the high fidelity model. This procedure may be useful in several circumstances including placing the safety box in an optimal location inside the SPOUA. This allows one to optimize the available space and minimize the casualty risk. This in turn also provides the optimal DEO point to aim for with the targeting algorithm [12]. This generalization procedure can be useful during the mission operations. For example, the optimal DEO point may need to be changed if more accurate density forecasts become available. The safety box depends on the expected density profile and the distribution of that density profile. If the density profile changes, the optimal safety box will change. Also, if the satellite is close to the de-orbit time, there may no longer be sufficient controllability left to target the desired DEO point. In that case, a new optimal DEO point can be picked from the set of reachable DEO points. Also, after observing the spacecraft in orbit, a more accurate estimate of the spacecraft ballistic coefficient can be obtained which will also affect the location of the optimal DEO point.

7.2. Generalization of the errors

When we set a different DEO point to be reached through the targeting algorithm, it may provide slightly different distributions of the errors at the DEO point both in terms of mean value and dispersions around the mean value. In Refs. [11,12], some convergence results as well as a general MC analysis is provided. Nevertheless, as long as the DEO point keeps the same altitude and the latitude and longitude vary within a neighborhood of the initial ones, these differences are not very significant. Additional analysis has been performed in this study showing that the only effects which should be taken into account are the variations of the mean values of the velocity magnitude v_{DEO} and the flight path angle γ_{DEO} with the DEO point geodetic latitude ζ_{DEO}. They can be linearly approximated as:

$$\mu'_{v_{DEO}} = \mu_{v_{DEO}} + 0.24\frac{m/s}{\text{deg}}\left(\zeta'_{DEO} - \zeta_{DEO}\right) \tag{32}$$

$$\mu'_{\gamma_{DEO}} = \mu_{\gamma_{DEO}} + 2.6 \times 10^{-3}\left(\zeta'_{DEO} - \zeta_{DEO}\right) \tag{33}$$

where ζ_{DEO} is the initial geodetic latitude for which the errors have been characterized through the MC analysis of the targeting algorithm (see sec.3.1) and ζ'_{DEO} is the new geodetic latitude where we want to set the DEO point. The linear fitting is justified in Fig. 16. Similar relationships

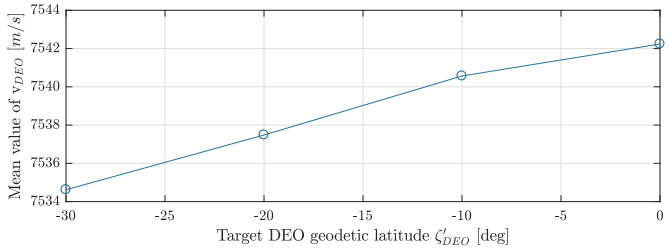

(a) Relative velocity magnitude at the DEO point.

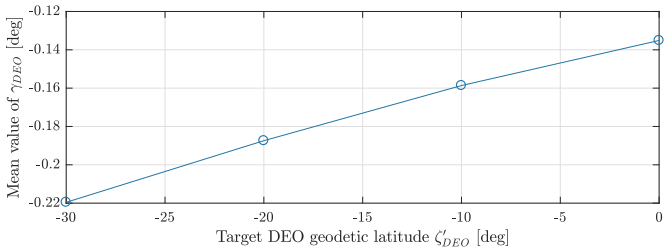

(b) Flight path angle at the DEO point.

Fig. 16. Average relative velocity magnitude and flight path angle vs. DEO point geodetic latitude.

may apply to other variables of the reduced order model, but the magnitudes of these variations are very small and can be neglected since they do not have a significant effect on the safety box dimensions.

It is very important to highlight that the above relations are valid when the DEO point is kept at the same geodetic altitude. The flight path angle and the velocity magnitude profiles significantly change when the DEO point altitude is varied. This must be taken into account to reliably estimate the safety box. Changing geodetic latitude and longitude but keeping the same altitude can be done exploiting some algebraic relations derived by Vallado in Ref. [42] and spherical trigonometry. For the sake of completeness, we briefly describe this transformation. Given the new geocentric latitude φ'_{DEO} and the altitude h_{DEO}, the new geodetic latitude can be computed by solving the following non-linear equation using a root finder:

$$\tan\varphi'_{DEO} = \tan\zeta'_{DEO}\left(1 - \frac{e_\oplus^2}{1 + h_{DEO}/R_\oplus\sqrt{1 - e_\oplus^2\sin^2\zeta'_{DEO}}}\right) \tag{34}$$

where $R_\oplus$ is the equatorial radius of Earth (6378.1363 km) and $e_\oplus = 0.081819$ is its eccentricity. The new distance from Earth center is computed as:

$$r'_{DEO} = \frac{\cos\zeta'_{DEO}}{\cos\varphi'_{DEO}} \tag{35}$$

The new argument of latitude u'_{DEO} is calculated keeping the same branch of the trajectory, descending or ascending, with respect to the initial DEO trajectory. This means

$$u'_{DEO} = \pi - \sin^{-1}\left(\frac{\sin\varphi'_{DEO}}{\sin i}\right) \quad \text{if } \pi/2 < \text{mod}(u_{DEO}, 2\pi) < 3\pi/2 \tag{36}$$

$$u'_{DEO} = \sin^{-1}\left(\frac{\sin\varphi'_{DEO}}{\sin i}\right) \quad \text{otherwise} \tag{37}$$

where i is the orbital inclination. Assuming the same orbital eccentricity $e' = e$ and the same orbital flight path angle[1] $\delta'_{DEO} = \delta_{DEO}$, we get that the true anomaly must also be the same: $\theta'_{DEO} = \theta_{DEO}$. So the new argument of perigee ω' is:

$$\omega' = u'_{DEO} - \theta'_{DEO} \tag{38}$$

and the new orbital semi-major axis is:

$$a' = \frac{r'_{DEO}(1 + e'\cos\theta'_{DEO})}{1 - e'^2} \tag{39}$$

Imposing a latitude change inevitably results in a longitude change. To set the desired longitude λ'_{DEO}, we set the new right ascension of the ascending node Ω' as:

$$\Omega' = \lambda'_{DEO} - \text{sign}\left(\frac{\tan\varphi'_{DEO}}{\tan i}\right)\cos^{-1}\left(\frac{\cos u'_{DEO}}{\cos\varphi'_{DEO}}\right) + \theta_{sid} \tag{40}$$

where θ_{sid} is the sidereal angle (e.g. from the vernal equinox to the foot of the Greenwich meridian in the equatorial plane).

7.3. Convergence procedure

The objective now is to iteratively move the DEO point to optimize the safety box inside the SPOUA. This procedure can be divided into three steps:

7.3.1. Computation of the desired AIP

The minimum latitude where the safety box can be placed is equal to minus the orbital inclination. If this does not exceeds the SPOUA lower bound (60deg South), as in the case study under analysis (orbital inclination $i = 51.9$deg), a good option is to place the center of the safety box as far South as possible. This constraint can be enforced setting the desired argument of latitude of the safety box center, let us call it $u_{MID_{Des}}$, to $3/2\pi$. Consequently, the desired argument of latitude for the AIP can be computed as:

$$u_{AIP_{Des}} = u_{MID_{Des}} - \frac{\text{D-range} + \text{U-range}}{2R_\oplus} \tag{41}$$

Eq (41) assumes that the A-range does not vary significantly when changing the DEO point for the same probability level. This is not actually true, but it is a good initial guess that will be corrected later. For the following computations, we consider $\alpha = 10^{-4}$, corresponding to D-range= 2810 km and U-range= −1330 km from Table 5. Thus, we get that $u_{AIP_{Des}} = 263.35$deg. Similarly, to optimize the SPOUA width, the longitude of the safety box center $\lambda_{MID_{Des}}$ is set in the middle of the SPOUA, corresponding to the 230deg East meridian. Consequently, the desired longitude of the AIP $\lambda_{AIP_{Des}}$ is computed as:

$$\lambda_{AIP_{Des}} = \lambda_{MID_{Des}} - \text{sign}\left(\frac{\tan\varphi_{MID_{Des}}}{\tan i}\right)\cos^{-1}\left(\frac{\cos u_{MID_{Des}}}{\cos\varphi_{MID_{Des}}}\right) + \\ + \text{sign}\left(\frac{\tan\varphi_{AIP_{Des}}}{\tan i}\right)\cos^{-1}\left(\frac{\cos u_{AIP_{Des}}}{\cos\varphi_{AIP_{Des}}}\right) \tag{42}$$

where $\varphi_{AIP_{Des}}$ is the desired geocentric latitude for the AIP, computed as:

$$\varphi_{AIP_{Des}} = \sin^{-1}(\sin i \sin u_{AIP_{Des}}) \tag{43}$$

and $\varphi_{MID_{Des}}$ is the desired geocentric latitude of the safety box center. In this case, $\varphi_{MID_{Des}} = -i = -51.9$deg, $\varphi_{AIP_{Des}} = -51.41$deg, and $\lambda_{AIP_{Des}} = 219.30$deg.

If a specific desired point is already available because other constraints are imposed (e.g. maximizing distance from a determined island, re-entry observation constraints, operational constraints, etc.) this initial step of the procedure can be avoided.

7.3.2. First DEO correction

When the DEO latitude changes, it affects both the latitude and longitude of the AIP. However, a longitude variation of the DEO point does not affect significantly the latitude of the AIP. Therefore, an efficient way to converge to the desired AIP is to correct for the latitude

[1] The orbital flight path angle is indicated with the symbol δ to not confuse it with the relative flight path angle γ, introduced in sec.3.1.

[2] Truncated at 11.3deg.

first. When the convergence is achieved, the remaining longitude error can be corrected, too. Let us describe this first convergence scheme. At the k-th step, the high fidelity model is propagated in time starting from the k-th DEO point having argument of latitude u_{DEO}^k up to ground impact. The geocentric latitude φ_{Imp}^k, longitude λ_{Imp}^k and sidereal time θ_{sidImp}^k are computed at the impact point. Thus, the argument of latitude is obtained as:

$$u_{Imp}^k = \pi - \sin^{-1}\left(\frac{\sin\varphi_{Imp}^k}{\sin i}\right) \quad \text{if } \pi/2 < \text{mod}\left(\lambda_{Imp}^k - \Omega + \theta_{sidImp}^k, 2\pi\right) < 3\pi/2 \tag{44}$$

$$u_{Imp}^k = \sin^{-1}\left(\frac{\sin\varphi_{Imp}^k}{\sin i}\right) \quad \text{otherwise} \tag{45}$$

where Ω is the orbital right ascension of the ascending node. The error is estimated with respect to the desired argument of latitude. So, at the k-th step it is:

$$Err_u^k = u_{AIP_{Des}} - u_{Imp}^k \tag{46}$$

The new iteration is initiated calculating the argument of latitude at the DEO point as:

$$u_{DEO}^{k+1} = u_{DEO}^k + Err_u^k \tag{47}$$

This introduces the assumption that the variation of the argument of latitude between impact and DEO point remains the same when the DEO point is changed. Again, this is not completely true, but is a reasonable assumption that verifies at convergence. The new geocentric latitude at the DEO point is:

$$\varphi_{DEO}^{k+1} = \sin^{-1}\left(\frac{\sin i}{\sin u_{DEO}^{k+1}}\right) \tag{48}$$

and the new longitude is:

$$\lambda_{DEO}^{k+1} = \lambda_{DEO}^k + \text{sign}\left(\frac{\tan\varphi_{DEO}^{k+1}}{\tan i}\right)\cos^{-1}\left(\frac{\cos u_{DEO}^{k+1}}{\cos\varphi_{DEO}^{k+1}}\right) - \text{sign}\left(\frac{\tan\varphi_{DEO}^k}{\tan i}\right)\cos^{-1}\left(\frac{\cos u_{DEO}^k}{\cos\varphi_{DEO}^k}\right) \tag{49}$$

These two inputs fully define the new DEO point that occurs at the same geodetic altitude as the previous DEO point. The associated state vector can be defined as described in the sec.7.2. The convergence is reached when the absolute value of Err_u^k becomes smaller than a given tolerance, set here to 1deg. After that, the DEO latitude is kept constant ($\varphi_{DEO}^{k+1} = \varphi_{DEO}^k$) and a second convergence scheme is set up to eliminate the remaining longitude error. The longitude error is computed as:

$$Err_\lambda^k = \lambda_{AIP_{Des}} - \lambda_{Imp}^k \tag{50}$$

and the new longitude at the DEO point is:

$$\lambda_{DEO}^{k+1} = \lambda_{DEO}^k + Err_\lambda^k \tag{51}$$

The procedure is stopped when $|Err_\lambda^k| < 0.5$deg. The final obtained φ_{DEO}^{k+1} and λ_{DEO}^{k+1} locate the optimal DEO point, in this case $\varphi_{DEO}^{Opt} = -5.69$deg and $\lambda_{DEO}^{Opt} = 150.03$deg. The convergence rate is rather fast. In this case, a total of 4 steps were necessary: 2 for the argument of latitude convergence and 2 for the longitude convergence. The re-entry trajectories obtained at each step are plotted in Fig. 17a. In Fig. 17b, the decreases of the absolute values of the errors along the iteration steps are given.

7.3.3. Verification of the safety box location

The assumption that the A-range magnitude remains constant when the DEO point is changed is now verified. To do this, a modified Single Step algorithm of the Inputs' Statistics method is utilized with the new optimal DEO point. The Single Step algorithm requires determining the probability outside the contour lines (e.g. ellipsoids) of the input pdf and computing the output interval as min/max inside the contour associated with the prescribed probability. In the basic version of the Single Step method, the decided probability coincides with the probability of interest and this guarantees a conservative result [49,52]. However, if a more accurate estimation of this probability is already available, it can be used to get a more accurate result. The idea is to exploit the convergence information of the Multistep algorithm for a given DEO point for any other DEO point. The α^k value computed with the Multistep iterations (see Fig. 15a) provides exactly what we are looking for: the probability outside the pdf contours at the k-step. The value of α^k at convergence is therefore used as the probability to be constrained in the Single Step algorithm. Thus, only two optimization processes are necessary to estimate the safety box associated with a new DEO point. This implies that once a safety box is computed for a given probability, it can be used to compute the safety box for any other DEO point reasonably close to the initial one and with the same geodetic altitude with only a few minutes of computational time. The assumption of a constant α^k at convergence is justified by the idea at the basis of the Inputs' Statistics method of using the pdf contours to approximate the contours of the transfer function. The error due to this approximation depends on the contours shape and so on the problem under analysis rather than on the specific initial condition used. In Fig. 18, we show in light blue the safety box shifted to the optimal AIP estimated from the initial DEO point. The safety box plotted in black is estimated instead with this modified Single Step approach, with $\alpha^k = 0.1453$ and starting from the optimal DEO point. Finally, we restarted the full statistical characterization of the optimal DEO point through an MC analysis of both the targeting algorithm (as seen in sec.3.1) and of the high fidelity model (in sec.3.2), and we ran the Multistep algorithm using the reduced order model as described in sec.6. The resulting safety box is plotted in green. We can draw the following conclusions:

- comparing the safety boxes in light blue and in black proves the quality of the assumption that the A-range remains constant when the DEO point is changed. If instead a significant difference existed, the entire procedure could be repeated with the new A-range estimation. It is expected that at most at the second iteration the two safety boxes will be very close to each other and the procedure will have converged. Note that re-running the procedure again does not require significant computational time since the MC analysis is not required and the Multistep algorithm is not necessary with the modified Single Step approach.
- comparing the safety boxes in black and green proves the accuracy of the modified Single Step approach and confirms that there is no need to re-run the Multistep algorithm. In addition, the small difference between the optimal AIP and the corrected AIP shows that the linear fittings of the mean values of the GNC errors given by eq. (32) and eq. (33) are good approximations and that it is not necessary to re-characterize the new DEO point through an MC analysis of the targeting algorithm.

8. Maximum probability of failure

Inverting eq. (21) for the mission casualty risk introduced in sec.5, the maximum admissible probability of control failure can be computed as function of the probability associated with the safety box as:

$$P_f \leq \frac{10^{-7}/E_n - \alpha}{1 - \alpha} \tag{52}$$

P_f depends on DEO point altitude, because a higher altitude results in a greater dispersion of the fragments as they fall through the atmosphere and hence a larger safety box. Looking at the problem in a reversed sense, for the largest safety box that still fits inside the SPOUA, the probability α that some fragments will fall outside the box will increase

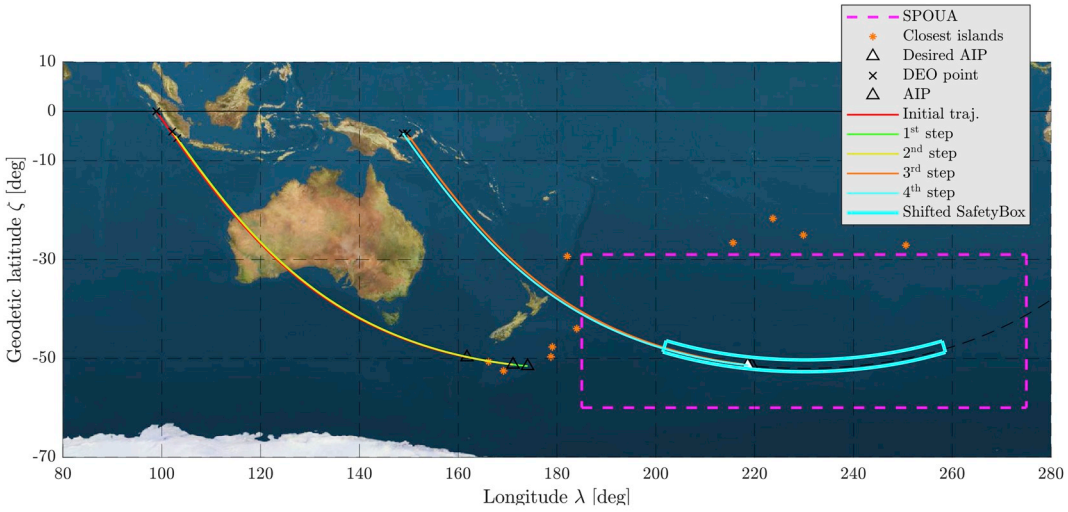

(a) Re-entry trajectories from DEO point to impact point

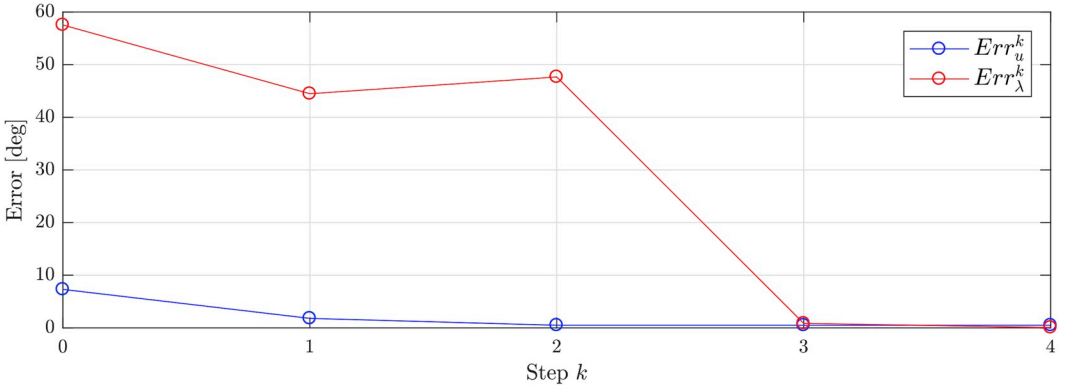

(b) Errors convergence.

Fig. 17. Convergence procedure to achieve a desired AIP location.

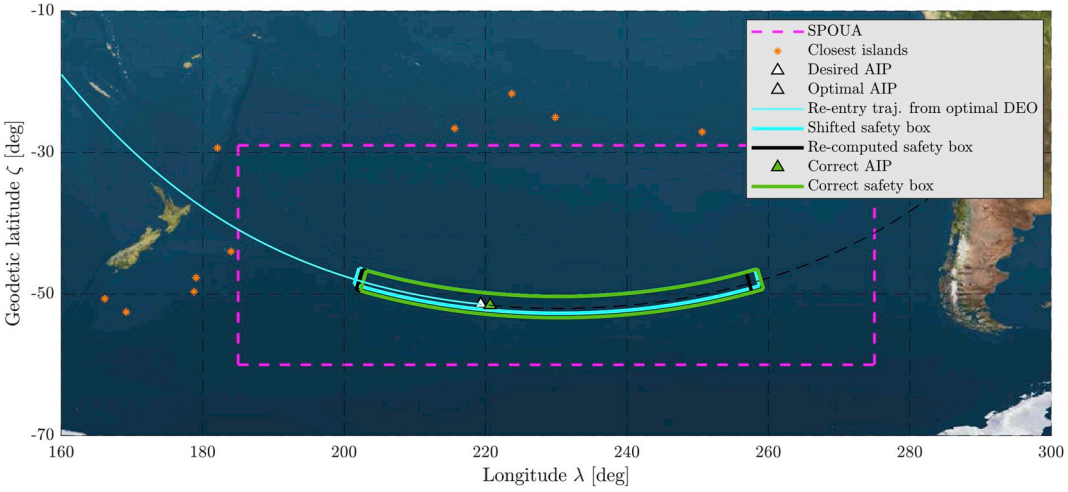

Fig. 18. Re-entry trajectories from DEO point to impact point.

as the DEO altitude increases. Therefore, for a given DEO altitude, there will be a maximum admissible probability of control failure to be compliant with the safety requirement. In this section, we describe a 5 steps procedure to obtain a reliable estimate of this maximum probability. The procedure takes advantage of both the Single Step and the Multistep algorithms of the Inputs' Statistics method to speed up the computation and utilizes the convergence procedure described in sec.7 to fit the safety box within the SPOUA. The procedure has to be repeated for any DEO altitude for which the computation of the maximum admissible probability of control failure is required.

8.1. Boundaries for $\alpha_{//}$

Since the A-range is much larger than the C-range as proven in sec.6, the largest admissible safety box is computed by determining when the A-range exceeds the SPOUA width. Therefore, the probability of interest in the following computations is the probability outside the A-range, indicated with $\alpha_{//}$. In sec.6.3, $\alpha_{//}$ was related (conservatively) to the overall probability outside the safety box as $\alpha_{//} = 0.1\alpha$. The largest $\alpha_{//}$ that is necessary to consider is the one that makes P_f equal to zero, that is $\alpha_{//}^{Max} = 0.1(10^{-7}/E_n)$. The DEO altitude that corresponds to this $\alpha_{//}$ limit is the theoretical maximum altitude that can be targeted (if $P_f = 0$) while still respecting the safety requirement. In a real case, the maximum DEO altitude will be less according to the minimum probability of control failure that the mission can guarantee. In contrast, there is no well defined limit for the smallest $\alpha_{//}$, but very small $\alpha_{//}$ values have almost no influence on the P_f computation. This is because when $\alpha_{//}$ is small, the casualty risk associated with fragments falling outside the SPOUA is not significant compared to the risk associated with a potential of control failure. This is true when $10^{-7}/E_n \gg \alpha$, so we set $\alpha_{//}^{Min} = 10^{-3}(10^{-7}/E_n)$.

8.2. Computation of a safety box exceeding the SPOUA through the Single Step algorithm

Starting from an initial guess of the optimal DEO point, the Single Step algorithm is applied iteratively to obtain an initial estimate for the probability outside the pdf contours α^j that provides a safety box exceeding the SPOUA. Starting with $\alpha^0 = \alpha_{//}^{Max}$ and decreasing it progressively as:

$$\alpha^{j+1} = \frac{\alpha^j}{10} \tag{53}$$

the A-range is computed at each iteration j. If $\alpha^j \leq \alpha_{//}^{Min}$ and A-range^j is still smaller than the maximum A-range admissible for the SPOUA, than the probability of a fragment landing outside the maximum admissible safety box is so small compared to $(10^{-7}/E_n)$ that it can be neglected and the iterative procedure can be stopped. In this case $P_f \simeq (10^{-7}/E_n)$. If $\alpha^j \geq \alpha_{//}^{Min}$ and A-range^j is greater than A-range^{max}, α^j is a conservative estimate for $\alpha_{//}$ and can be used in the next step.

8.3. First estimation of $\alpha_{//}$ through the multistep algorithm

The value of α^j estimated at the last step of the previous iterative process guarantees an A-range larger than the A-range^{max}. Therefore, using it as initial value for the Multistep algorithm, the A-range is progressively decreased at each iteration k and the probability of debris falling outside the A-range^k is estimated. Let us call this probability $\mathbb{P}^{IS^k}$ in accordance with the nomenclature in Ref. [43]. The process will eventually converge to an estimate of the A-range such that $\mathbb{P}^{IS^k} \simeq \alpha^j$. However, it is forced to stop prematurely as soon as the A-range^k becomes smaller than the A-range^{max}. Thus, A-range^k is the largest one that can fit within the SPOUA and the associated $\mathbb{P}^{IS^k}$ is a good initial estimate of $\alpha_{//}$. If $\mathbb{P}^{IS^k} \ll \alpha_{//}^{Min}$, we can approximate $\alpha_{//}$ as zero and P_f as $(10^{-7}/E_n)$. If $\alpha^j = \alpha_{//}^{Max}$ and $\mathbb{P}^{IS^k} \leq \alpha_{//}^{Min}$ without satisfying the condition A-range^k < A-range^{max}, then $\alpha_{//} \geq \alpha^{Max}$ and P_f can be approximated as 0. In all cases where the algorithm terminates prematurely and $\alpha_{//}^{Min} < \mathbb{P}^{IS^k} < \alpha_{//}^{Max}$, the probability outside the current pdf contour α^k as well as the U-range^k and the D-range^k associated with the A-range^k are stored and used in the following steps.

8.4. Computation of the optimal DEO point

In the previous steps, the safety box associated with A-range^k is obtained from a DEO point which may not be the optimal one, so it is likely that the D-range exceeds the SPOUA. An example of the safety box corresponding to such a DEO point is shown in red in Fig. 19 for the case of $h_{DEO} = 124\ km$. Using the convergence procedure described in sec.7 and the new values of U-range^k and D-range^k, the optimal DEO point can be computed such that the safety box fits within the SPOUA as shown in yellow in Fig. 19. Subsequently, the values of U-range^k and D-range^k can be corrected as shown in green in Fig. 19 through the modified Single Step algorithm starting from the previously estimated α^k.

8.5. Final estimation of $\alpha_{//}$ through MC simulation

A MC simulation can be performed to precisely estimate $\mathbb{P}^{IS^k}$ with the prescribed confidence level and relative error. The number of required sample trajectories N is computed through eq. (18) using the previous estimate of $\mathbb{P}^{IS^k}$. Only those samples that fall outside the pdf contour $\tilde{\varepsilon}^k$ associated with α^k are actually simulated. In addition, if the N^k samples previously simulated with the Multistep algorithm are stored, it is only necessary to simulate another $\alpha^k N - N^k$ samples. After the simulations, $\mathbb{P}^{IS^k}$ is computed by counting the number of samples that fall after D-range^k or before U-range^k and dividing by N. Thus $\mathbb{P}^{IS^k}$ is a reliable estimate of $\alpha_{//}$. The final estimate of the probability α of debris falling outside the largest safety box that can be fit within the SPOUA for a given DEO altitude is then simply computed as: $\alpha = 10\,\mathbb{P}^{IS^k}$. Finally, eq. (52) provides the maximum permissible probability of failure P_f that yields a casualty risk less than 10^{-7} for that specific DEO altitude.

In conclusion, the computational time required by this procedure to compute P_f for a specific DEO altitude is equal to the time that would be required by the Multistep algorithm to estimate a probability on the order of $\mathbb{P}^{IS^k}$ for a specified confidence level and relative error. Since $\mathbb{P}^{IS^k}$ is quite small for low DEO altitudes, this procedure is significantly more efficient than the CMC. We have repeated this computation for several values of DEO altitudes and the resulting P_f values are shown in Fig. 20. Given a specific mission with a predetermined P_f, Fig. 20 provides the maximum DEO altitude that can be targeted to meet the safety requirement.

9. Conclusions

This paper presents a safety analysis framework, based on the geometrical concept of safety boxes, for the estimation of the casualty risk resulting from a small satellite performing a controlled destructive atmospheric re-entry. A high fidelity model is developed to estimate the aerodynamic and aerothermodynamic interaction of the spacecraft with the airflow. Several uncertainties exist in this model, though, which are captured by 50 uncertain variables. These uncertainties can be condensed in a set of 12 high level variables that are able to fully describe the fragmentation process and the re-entry dynamics. These variables are used in a reduced order model that can be simulated with a computational time one order of magnitude smaller (0.7 s compared to 30 s evaluated on the same standard desktop computer) than the time required by the high fidelity model. The average location of the ground impact point predicted by the reduced order model differed from that predicted by the high fidelity model by only 50 km in the down track

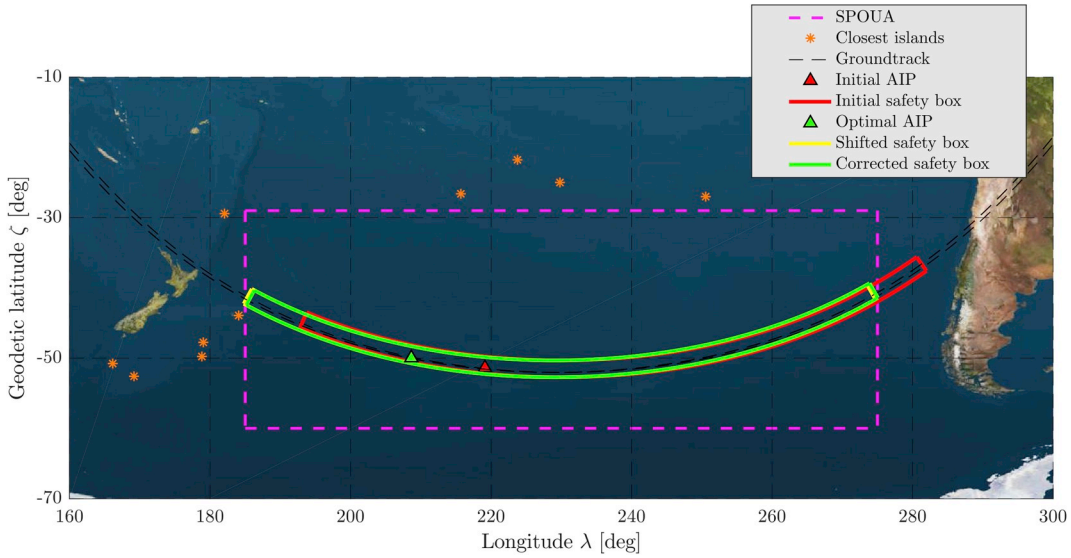

Fig. 19. Correction of the maximum safety box that can be fitted within the SPOUA starting from 124 *km* DEO altitude.

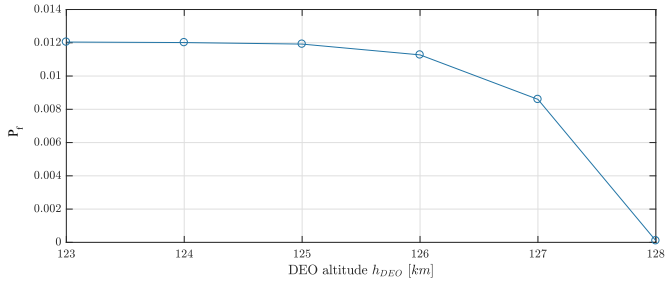

Fig. 20. Maximum probability of control failure admissible to meet the safety requirement.

direction. Through a low budget (3460 samples) Monte Carlo analysis of the high fidelity model, the high level variables can be statistically characterized. Simple linear fittings are utilized to generalize their errors for any de-orbit (DEO) point with the same geodetic altitude without needing to re-perform the Monte Carlo analysis of the high fidelity model. The reduced order model is coupled with the Inputs' Statistics method to obtain the estimate of very low probabilities within a reasonable computational time. Considering a confidence level of 95% with 10% relative error, only about 15 %– 4% of the samples of a Crude Monte Carlo method will be required when using the Inputs' Statistic method to compute probabilities on the order of $10^{-4} - 10^{-5}$. The computational time required to estimate a probability of 10^{-5} for this problem is thus reduced from a hypothetical 10 months for the Crude Monte Carlo to 12 days, with the possibility of parallelizing the computation.

In addition, a convergence procedure is suggested to target an optimal Aimed Impact Point in order to place the safety box perfectly in the middle of the South Pacific Ocean Uninhabited Area (SPOUA). This convergence procedure exploits a modified version of Single Step algorithm of the Inputs' Statistics method and is computationally inexpensive (few minutes). The procedure is therefore able to compute the latitude and longitude of the optimal DEO point that can be provided as an input to the de-orbit point targeting algorithm to minimize the casualty risk for a specific re-entry scenario. Finally, using this convergence procedure and the Multistep algorithm of the Inputs' Statistics method, it is possible to set up an iterative procedure to estimate the probability of a debris fragment landing outside the largest possible safety box that can fit within the SPOUA. This probability is related with an inequality constraint to 1) the casualty risk of uncontrolled re-entry estimated to be 8.3×10^{-7} in this 2U CubeSat case study, 2) the maximum allowable casualty probability for the mission, considered to be 10^{-7}, and 3) the maximum probability of failure to control the spacecraft to the desired DEO point. The maximum probability of failure is estimated for different DEO altitudes. The maximum theoretical DEO altitude that could be targeted such that the casualty risk is below 10^{-7} if the mission is able to guarantee a zero probability of failure is 128 *km*. With a reasonable value of 0.01 probability of failure, the mission will be compliant with the safety requirement as long as the optimal DEO location at an altitude below 125 *km* is targeted.

References

[1] NASA, Process for limiting orbital debris, Tech. rep. (2012) NASA-STD 8719.14 Revision A with Change 1.
[2] R.C. Reynolds, A. Soto, Debris Assessment Software, Operators Manual, Tech. rep., NASA Lyndon B, Johnson Space Center, 2001.
[3] E.S. WG, ESA space debris mitigation compliance verification guidelines, ESSB-HB-U-002-Issue1, from Inter-Agency Space Debris Coordination Committee website, 2015. http://www.iadc-online.org/.
[4] CubeSat Design Specification Rev. 13, Tech. rep., the CubeSat Program, California Polytechnic State University, San Luis Obispo, 2014.
[5] F. Renaud, T. Martin, Safety boxes sizing for controlled Re-entry application to automated transfer vehicle (ATV), Proceedings of the 3rd IAASS Conference: Building a Safer Space Together, 21-23 October 2008 Rome, Italy.
[6] J. Dobarco-Otero, R.N. Smith, K.J. Bledsoe, R.M. Delaune, W.C. Rochelle, N. Johnson, The object reentry survival analysis tool (ORSAT)-version 6.0 and its application to spacecraft entry, Proceedings of the 56th Congress of the International Astronautical Federation, the International Academy of Astronautics, Vol. 3 International Institute of Space Law, 2005, pp. 17–21 IAC-05-B6.
[7] W.C. Rochelle, B. Kirk, B.C. Ting, User's Guide for Object Reentry Survival Analysis Tool (ORSAT), Verison 5.0, Vols. I and II, Tech. Rep, (July, 1999) JSC-28743.
[8] G. Koppenwallner, B. Fritsche, T. Lips, H. Klinkrad, SCARAB - a multi-disciplinary code for destruction analysis of space-craft during re-entry, 5th European Symposium on Aerothermodynamics for Space Vehicles, Vol. 563 2005, p. 281.
[9] C. Hourtolle, S. Delattre, J.-F. Goester, E. De Pasquale, Studies about a shallow Re-entry for ATV-5, 25th International Symposium on Space Flight Dynamics, 19–23 October, 2015 Munich, Germany.
[10] E. De Pasquale, M. Steinkopf, L. Francillout, I. Escane, P. Benarroche, S. Delattre, L. Arzel, ATV shallow reentry mission: challenges and achievements, in: 8th Aerothermodynamics Symposium for Space Vehicles, 2-6 March 2015, Lisbon, Portugal.
[11] S.R. Omar, R. Bevilacqua, D. Guglielmo, L. Fineberg, J. Treptow, S. Clark, Y. Johnson, Spacecraft deorbit point targeting using aerodynamic drag, J. Guid. Contr. Dynam. 40 (10) (2017) 2646–2652.
[12] S. Omar, R. Bevilacqua, A Hybrid adaptive control algorithm for spacecraft guidance tracking using aerodynamic drag, 1st IAA Conference on Space Situational Awareness, ICSSA, Orlando, FL, USA, 2017.
[13] J. Virgili, P. Roberts, Atmospheric interface reentry point targeting using aerodynamic drag control, J. Guid. Contr. Dynam. 38 (3) (2015) 1–11, https://doi.org/10.2514/1.G000884.
[14] S. Dutta, A. Bowes, A.M. Dwyer Cianciolo, C. Glass, R.W. Powell, Guidance scheme

for modulation of drag devices to enable return from low Earth orbit, AIAA Atmospheric Flight Mechanics Conference, 2017, p. 0467 http://arc.aiaa.org/doi/pdf/10.2514/6.2017-0467.
[15] D. Guglielmo, S. Omar, R. Bevilacqua, Drag de-orbit device: a new standard re-entry actuator for CubeSats, 1st IAA Conference on Space Situational Awareness, ICSSA, Orlando, FL, USA, 2017.
[16] D. Guglielmo, R. Bevilacqua, Propellant-less atmospheric differential drag LEo spacecraft (PADDLES) mission, Proceedings of the 2014 SmallSat Conference, 2014 http://riccardobevilacqua.com/Guglielmo_Student_Paper.pdf.
[17] J.D. Anderson Jr., Hypersonic and High Temperature Gas Dynamics, McGraw Hill Series in Aeronautical and Aerospace Sciences, 1989.
[18] J.J. Bertin, Hypersonic Aerothermodynamics, AIAA Education Series, 1994.
[19] S.F. Rafano Carnà, R. Bevilacqua, High fidelity model for the atmospheric re-entry of CubeSats equipped with the Drag De-Orbit Device, accepted for publication in Acta Astronautica, https://doi.org/10.1016/j.actaastro.2018.05.049, (2018).
[20] T. Lips, B. Fritsche, A comparison of commonly used re-entry analysis tools, Acta Astronaut. 57 (2) (2005) 312–323.
[21] E.R. Van Driest, The problem of aerodynamic heating, Aeronautical Engineering Review (1956) 26–41.
[22] N.X. Vinh, A. Busemann, R.D. Culp, Hypersonic and Planetary Entry Flight Mechanics, ANN Arbor The university of Michigan press, 1980 Chapter 2.
[23] F. W. Matting, Approximate bridging relations in the transitional regime between continuum and free-molecule flows, J. Spacecraft Rockets 8.
[24] H. Legge, Hypersonic approximations for heat transfer and shear stress applied to continuum and rarefied plume impingement, DFVLR-IB 222–87 A23 (1987).
[25] E.R. Eckert, Survey of Boundary Layer Heat Transfer at High Velocities and High Temperatures, Tech. rep., WADC Technical Report 55-624, Minnesota University, 1960.
[26] S.A. Schaaf, P.L. Chambre, Flow of Rarefied Gases, High Speed Aerodynamics and Jet Propulsion, Vol. III, Fundamentals of Gas Dynamics, Princeton University Press, NY, 1958.
[27] L. Lees, Hypersonic flow, 5th International Aeronautical Conference, Los Angeles, California, 1955, pp. 241–276.
[28] J.A. Fay, F.R. Riddell, Theory of stagnation point heat transfer in dissociated air, J. Aeronaut. Sci. 25 (2) (1958) 73–85.
[29] E.R.G. Eckert, Engineering relations for friction and heat transfer to surfaces in high velocity flow, J. Aeronaut. Sci. 22 (8) (1955) 585–587.
[30] D. Guglielmo, S.R. Omar, R. Bevilacqua, L. Fineberg, J. Treptow, B. Poffenberger, Y. Johnson, Drag De-orbit Device (D3): a Retractable Device for CubeSat Attitude and Orbit Control Using Aerodynamic Forces, Orlando, FL, (2017).
[31] J. Morio, M. Balesdent, Estimation of Rare Event Probabilities in Complex Aerospace and Other Systems, Woodhead Publishing, 2015.
[32] F.J. Massey, The Kolmogorov-smirnov test for goodness of fit, J. Am. Stat. Assoc. 46 (253) (1951) 68, https://doi.org/10.2307/2280095 http://www.jstor.org/stable/2280095?origin=crossref.
[33] R. L. Ott, M. T. Longnecker, An Introduction to Statistical Methods and Data Analysis, fifth ed., Duxbury Thomson Learning.
[34] N.L. Johnson, S. Kotz, N. Balakrishnan, Continuous Univariate Distributions vol. 2, John Wiley & Sons, New York, 1995 Chapter 26.
[35] D.A. Vallado, D. Finkleman, A critical assessment of satellite drag and atmospheric density modeling, Acta Astronaut. 95 (2014) 141–165.
[36] D.G. King-Hele, R.R. Allan, The rotational speed of the upper atmosphere, Space Sci. Rev. 6 (2) (1966) 248–272.
[37] R.G. Wilmoth, R.A. Mitcheltree, J.N. Moss, Low-density aerodynamics of the stardust sample return capsule, J. Spacecraft Rockets 36 (3) (1999) 436–441.
[38] T.Y. Li, H.T. Nagamatsu, Hypersonic viscous flow on noninsulated flat plate, Proceedings of the 4th Midwestern Conf. On Fluid Mechanics, Purdue Univ, Lafayette, Ind, 1955, pp. 273–287.
[39] H.H. Hamilton, R.N. Gupta, J.J. Jones, Flight stagnation-point heating calculations on Aeroassist Flight Experiment vehicle, Journal of Spacecraft 28 (1) (1991) 125–127.
[40] B. Richard, Adaptive Control Processes: a Guided Tour, Princeton University Press, 1961.
[41] M. Picone, A.E. Hedin, D. Drob, Model 2001 of NRLMSISE-00, Empirical Model of the Atmosphere, Naval Research Laboratory, 2001, https://ccmc.gsfc.nasa.gov/modelweb/atmos/nrlmsise00.html.
[42] D.A. Vallado, Fundamentals of Astrodynamics and Applications 12 Springer Science & Business Media, 2001 Chapter 3.
[43] S.F. Rafano Carná, E. De Pasquale, L. Arzel, M. Lavagna, Reduction of the probability bias of the single step inputs' statistics method for the computation of the safety Re-entry area: introduction of a Multistep algorithm, 7th European Conference on Space Debris, ESA/ESOC, Darmstadt, Germany, 18-21 April 2017.
[44] G. Rubino, B. Tuffin, Rare Event Simulation Using Monte Carlo Methods, Wiley Online Library, 2009.
[45] N.L. Johnson, S. Kotz, N. Balakrishnan, Continuous Univariate Distributions vol. 1, John Wiley & Sons, New York, 1994 Chapter 13.
[46] A.W. Bowman, A. Azzalini, Applied Smoothing Techniques for Data Analysis: the Kernel Approach with S-plus Illustrations 18 Oxford Sciences Pubblications, Statistical Science Series, 1997.
[47] R. Lebrun, Contributions to Stochastic Dependence Modeling, Unpublished doctoral dissertation, Université Paris VII, Denis Diderot, 2013.
[48] T. R. of the French Space Act, Décrets, arrêtés, circulaires - textes Généraux, Art.23, Ministère de l'Enseignement Supérieur et de le Rcherche, J. Offic. de la République Français, from Inter-Agency Space Debris Coordination Committee website, http://www.iadc-online.org/(31 May 2011).
[49] E. De Pasquale, S. Rafano Carná, L. Arzel, M. Lavagna, Innovative method for the computation of Safety Re-entry Area based on the probability of uncertainties in the input parameters, 6th International Conference on Astrodynamics Tools and Techniques, ICATT, Darmstadt, Germany, 14-17 March 2016.
[50] J.N. Opiela, M.J. Matney, Improvements to NASA's estimation of ground casualties from reentering space objects, Sci. Technol. 109 (2004) 385–392 https://arc.aiaa.org/doi/pdf/10.2514/6.IAC-03-IAA.5.4.03.
[51] T. Vincenty, Direct and inverse solutions of geodesics on the ellipsoid with application of nested equations, Surv. Rev. 23 (176) (1975) 88–93.
[52] S.F. Rafano Carná, The Inputs' Statistics Method: an Innovative Method for the Computation of the Re-entry Safety Boxes with Application to the ATV-GL Shallow Re-entry, Tech. Rep, Master Thesis Politecnico di Milano, July 2016.
[53] G. Casella, R.L. Berger, Statistical inference, Duxbury Pacific Grove, CA, Vol. 2 2002.
[54] A. Nataf, Statistique mathematique-determination des distributions de probabilites dont les marges sont donnees, Compte Rendus de l'Académie des Sciences, in French 255 (1) (1962) 42–43.
[55] R. Lebrun, A. Dutfoy, An innovating analysis of the Nataf transformation from the copula viewpoint, Probabilist. Eng. Mech. 24 (3) (2009) 312–320.
[56] A. Quarteroni, F. Saleri, P. Gervasio, Scientific Computing with MATLAB® and Octave, fourth ed., Springer, New York, 2014.
[57] I. Newton, Philosophiæ Naturalis Principia Mathematica, London.
[58] F.C. Hulburt, Encyclopedia of Applied Physics,, Chap. Rarefied-gas Dynamics, Wiley-VCH Verlag GmbH & Co KGaA, 2003, pp. 97–115.

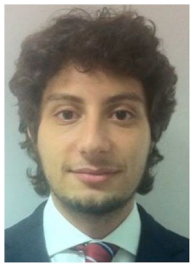

Simone Flavio Rafano Carná graduated in MS Space engineering at Politecnico di Milano, Italy, in 2016. He is currently a visiting researcher at the ADAMUS laboratory, at the University of Florida, Florida, USA. He has a working experience at the European Space Agency as Student Placement. As Flight dynamics Intern, he supported the ESA-OMT Flight Dynamics in the analysis of the atmospheric destructive re-entry of the Automated Transfer Vehicle - Georges Lamaître, developing an independent method for the re-entry safety boxes estimation, named Inputs' Statistics method. His research interests span from non linear space dynamics to atmospheric re-entry and uncertainty quantification.

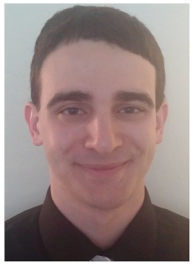

Sanny Omar is a PhD Candidate at the University of Florida. He graduated Summa Cum Laude with Honors from Auburn University in 2015 with a bachelor's degree in Aerospace Engineering and minors in business, Spanish, and computer science. He has conducted internships at GE Aviation and SpaceX and has been awarded the National Science Foundation Graduate Research Fellowship and NASA Space Technology Research Fellowship for his PhD studies. Sanny is also an instrument rated private pilot and a certified scuba diver. Sanny specializes in spacecraft dynamics and control and has extensive experience in controlling spacecraft orbits using aerodynamic drag.

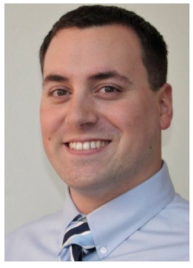

Dr. David Guglielmo is a postdoctoral researcher at the University of Florida (UF). His research combines spacecraft design and modeling, with a focus on CubeSats. While at UF for his doctoral work, Dr. Guglielmo completed the design of a 3U CubeSat with a repeatedly retractable drag sail, denoted PADDLES. In addition to work at UF, Dr. Guglielmo also earned his MS in Mechanical Engineering at Rensselaer Polytechnic Institute (RPI) with a focus in the manufacture and design of fuel cells.

Dr. Riccardo Bevilacqua is an Associate Professor of the Mechanical and Aerospace Engineering Department, at the University of Florida. He holds a M.Sc. in Aerospace Engineering (2002), and a Ph.D. in Applied Mathematics (2007), both from the University of Rome, "Sapienza", Italy. Dr. Bevilacqua is the recipient of two Young Investigator Awards, from the Air Force Office of Scientific Research (2012) and the Office of Naval Research (2013), of the 2014 Dave Ward Memorial Lecture Award from the Aerospace Controls and Guidance Systems Committee, and of two Air Force Summer Fellowships (2012 and 2015). His research interests focus on spacecraft formation flight and space robotics. He has authored and co-authored more than 60 journal and conference publications on the topic. Dr. Bevilacqua is a corresponding member of the IAA and an associate fellow of the AIAA.